AGU PUBLICATIONS

JGR

Journal of Geophysical Research: Oceans

RESEARCH ARTICLE

10.1002/2015JC011468

Pathways and mechanisms of offshore water intrusions on the Espírito Santo Basin shelf (18°S–22°S, Brazil)

A. Palóczy[1,2], K. H. Brink[3], Ilson C. A. da Silveira[1], Wilton Z. Arruda[4], and Renato P. Martins[5]

[1]Instituto Oceanográfico, Universidade de São Paulo, São Paulo, Brazil, [2]Now at Scripps Institution of Oceanography, University of California, San Diego, La Jolla, California, USA, [3]Woods Hole Oceanographic Institution, Woods Hole, Massachusetts, USA, [4]Instituto de Matemática, Universidade Federal do Rio de Janeiro, Rio de Janeiro, Brazil, [5]Centro de Pesquisas e Desenvolvimento Leopoldo Américo Miguez de Mello, Rio de Janeiro, Brazil

Key Points:
- South Atlantic Central Water intrusions occur at preferred locations south of 19°S
- Onshore geostrophic transport is important in both wind and Brazil Current-forced experiments
- Intrusions are forced primarily by wind and are enhanced by Brazil Current-related processes

Correspondence to:
A. Palóczy,
apaloczy@ucsd.edu

Citation:
Palóczy, A., K. H. Brink, I. C. A. da Silveira, W. Z. Arruda, and R. P. Martins (2016), Pathways and mechanisms of offshore water intrusions on the Espírito Santo Basin shelf (18°S–22°S, Brazil), *J. Geophys. Res. Oceans*, *121*, 5134–5163, doi:10.1002/2015JC011468.

Received 12 NOV 2015
Accepted 1 JUN 2016
Accepted article online 6 JUN 2016
Published online 30 JUL 2016

Abstract The pathways and physical mechanisms associated with intrusions of cold, nutrient-rich South Atlantic Central Water (SACW) on the continental shelf of the Espírito Santo Basin (ESB), off southeast Brazil (18°S–22°S), are investigated. To this end, a set of process-oriented, Primitive-Equation (PE) numerical models are used, together with an independent and more complete PE model, available observations and simple theoretical ideas. SACW enters the model ESB shelf mostly through two preferential pathways along the Tubarão Bight (TB, 19.5°S–22°S). These pathways are found to be locations where an equatorward along-isobath pressure gradient force (PGF_{y^*}) of $O(10^{-6}$ m s$^{-2})$ develops in response to steady wind forcing. This equatorward PGF_{y^*} is essentially in geostrophic balance, inducing onshore flow across the shelf edge, and most of the shelf proper. The Brazil Current (BC) imparts an additional periodic (in the along-shelf direction) PGF_{y^*} on the shelf. The intrinsic pycnocline uplifting effect of the BC in making colder water available at the shelf edge is quantified. The BC also induces local intrusions by inertially overshooting the shelf edge, consistent with estimated Rossby numbers of ≈0.3–0.5. In addition, the planetary β-effect is related to a background equatorward PGF_{y^*}. A modified Arrested Topographic Wave model is shown to be a plausible rationalization for the shelf-wide spreading of the pressure field imparted by the BC at the shelf edge. The deep-ocean processes examined here are found to enhance the onshore transport of SACW, while wind forcing is found to dominate it at leading order.

1. Introduction

The Espírito Santo Basin (ESB) is located in the western South Atlantic, within the Abrolhos-Campos Region (ACR, Figure 1a) [*Castro and Miranda*, 1998], slightly to the south of the site where the southern branch of the South Equatorial Current (sSEC) bifurcates, originating the Brazil Current (BC). At surface levels (0–200 m), within the domain of the warm and oligotrophic Tropical Water (TW, defined by *Mémery et al.* [2000] as water with practical salinity higher than 36), the sSEC bifurcation migrates seasonally within the 13°S–17°S range. At 200 m, within the domain of the cold and nutrient-laden South Atlantic Central Water (SACW, defined by the line connecting the temperature-practical salinity points 5°C, 34.3 and 20°C, 36.0), the sSEC bifurcates climatologically at 18.6°S, north of the Vitória-Trindade Ridge (VTR, Figure 1a) [*Stramma and England*, 1999; *Rodrigues et al.*, 2007].

At mesoscales, offshore of the shelfbreak, the ESB is dominated by a rich eddy field. According to *Soutelino et al.* [2011], three semipermanent anticyclones occupy the surroundings of the Abrolhos Bank (AB). To the south of the VTR, there is a transient cyclonic perturbation of the BC, known as the Vitória Eddy [*Schmid et al.*, 1995; *Campos*, 2006; *Arruda et al.*, 2013]. This scenario reveals a complex deep-ocean circulation in the ESB, which may have important effects on the intrusions of water with higher SACW content on the shelf. Hereafter, SACW will be taken to mean relatively colder and fresher water on the shelf (compared to the warmer and saltier TW).

Coastal waters between the AB and Cape São Tomé are dominated by the influence of the warm and salty TW year-round. In the AB, the TW occupies most of the volume of the continental shelf. To the south of the AB (21°S), the influence of the relatively colder and fresher SACW close to the bottom is intermittent. Such influence is most intense in the summer, when a sharp seasonal thermocline is established in response to the penetration of this oceanic water mass on the shelf [*Castro and Miranda*, 1998].

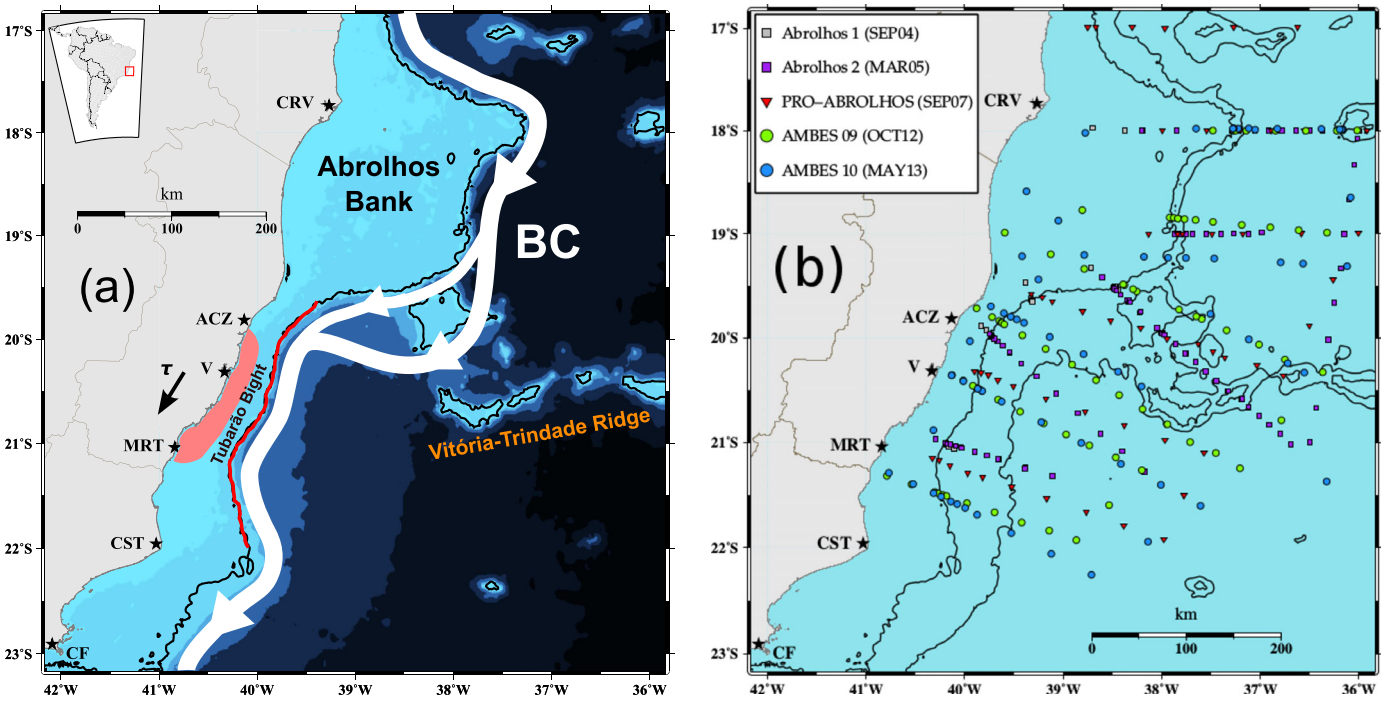

Figure 1. (a) Topographic map of the Espírito Santo Basin (ESB). The upper left map insert marks the location of the study area off the coast of South America (red rectangle). The locations marked by the black stars are Cape Frio (CF), Cape São Tomé (CST), Marataízes (MRT), Vitória (V), Aracruz (ACZ), and Caravelas (CRV). The red line indicates the domain of the Tubarão Bight (TB). The edges of the blue shadings are the 30, 500, 1000, 2000, 3000, and 4000 m isobaths, and the black line is the 100 m isobath. (b) Representation of the in situ quasi-synoptic data sets within the study region. The black lines are the 100 and 2000 m isobaths. Isobaths in both maps are derived from the 30 arc second SRTM30-plus data set (updated from *Smith and Sandwell* [1997]).

On the continental shelf, the main forcing in the AB is the wind, which is southwestward year-round, producing southwestward currents [*Castro and Miranda*, 1998]. Shelfbreak upwelling induced by internal tides seems to be important along the southern flank of the AB [*Pereira et al*., 2005], possibly contributing to the observed local nutrient enrichment [*Gaeta et al*., 1999]. North of the VTR, the newly formed BC flows mostly offshore, and has little effect on the shelf circulation. South of 19°S, however, *Castro and Miranda* [1998] point out that the BC occasionally follows the shelf edge, with a significant transport inshore of the shelfbreak area.

The first study to consider the dynamics of the coastal circulation under steady wind forcing in the ESB was carried out by *Rodrigues and Lorenzzetti* [2001]. Using process-oriented experiments with a two-layer numerical model, the authors addressed the effects of coastline geometry and bottom topography on the shelf circulation. They show that bottom topography is more important than coastline geometry in controlling the time-averaged coastal upwelling response in the Tubarão Bight (TB) area (19.5°S–22°S, Figure 1a). The more simplified analytical approach employed by *Mazzini and Barth* [2013] further clarified the upwelling mechanisms related to wind forcing and coastal geometry, by breaking down the vertical transport in two wind-forced components (coastal Ekman transport divergence and Ekman pumping) and two topographically forced components (shear vorticity and curvature vorticity). Specifically, they show that the TB is where the Ekman transport-forced upwelling is a maximum ($\approx$0.75 m^2 s^{-1}), accounting for nearly the entire (80%–100%) wind-driven transport. In addition, *Mazzini and Barth* [2013] estimate that wind-driven upwelling dominates over topographically driven upwelling in the TB, accounting for more than 75% of the total vertical transport. This also substantiates earlier observational results from *Castelão and Barth* [2006], confirming that the contribution of Ekman transport divergence is far more important to vertical transport in the TB than Ekman pumping.

Although deep-ocean forcing mechanisms related to the BC seem to be relevant to coastal upwelling south of the ESB [*Calado et al*., 2010; *Palóczy et al*., 2014], their effects within the ESB have only recently been examined by *Aguiar et al*. [2014]. These authors performed diagnostic analyses of a realistic primitive-

equation numerical model to quantify the upwelling contributions from Ekman transport, Ekman pumping, encroaching of the BC onto the shelf, and cyclonic BC meandering. They found that BC encroaching is generally more effective than cyclonic meanders in driving SACW intrusions within the TB. *Aguiar et al*. [2014] also point out that coastal Ekman transport divergence is the most effective forcing mechanism around 21°S, consistent with the previous findings of *Castelão and Barth* [2006] and *Mazzini and Barth* [2013]. However, quantification of the effects of the wind and the BC in terms of momentum balances has not yet been done for the ESB.

This regional overview shows that much remains to be learned on the SACW intrusion processes within the ESB. The aim of this study is to answer the following questions:

1. Are there preferential pathways for SACW penetration on the ESB shelf?
2. What physical mechanisms drive the subtidal cross-isobath circulation on the ESB shelf? Specifically, what are the individual and combined effects of bottom topography, wind-forcing, and the Brazil Current? What is the along-isobath momentum balance on the continental shelf?

The approach chosen consists of analyses of a set of process-oriented experiments done with a simplified primitive-equation numerical model, supported by analyses of an independent, more complete numerical model and available observations. We first describe the data sets in section 2 and the numerical models in section 3. Next, in section 4, we analyze the pathways through which SACW may enter the ESB shelf. We then address the dynamics linked to the intrusion process in section 5, and attempt to isolate and rationalize some of the physical mechanisms involved in section 6. We conclude by summarizing the primary results and presenting conclusions in section 7.

2. Data Sets

2.1. In Situ Quasi-Synoptic Data

The in situ data used in this study come from five quasi-synoptic oceanographic cruises: Abrolhos 1 (September, 2004), Abrolhos 2 (March, 2005), PRO-ABROLHOS (September, 2007), AMBES-09 (October, 2012), and AMBES-10 (May, 2013). Hereafter we will refer to these surveys as SEP04, MAR05, SEP07, OCT12, and MAY13, respectively. Surveys SEP04, MAR05, and SEP07 were carried out on the R/V Prof. *Wladimir Besnard*, while surveys OCT12 and MAY13 were carried out on the R/V *Seward Johnson*. The geographic distribution of the Conductivity, Temperature and Depth (CTD) stations of each survey is shown in Figure 1b. Hydrographic data from the CTD casts were processed following standard procedures [e.g., *McTaggart et al*., 2010].

2.2. Climatological Hydrographic Data

Climatological data from the World Ocean Atlas 2013 (WOA13) were used in the elaboration of the initial conditions of the process-oriented numerical experiments. The fields used in this study are the Temperature [*Locarnini et al*., 2013] and Salinity [*Zweng et al*., 2013] austral summer distributions, objectively analyzed to a 0.25° grid with 102 vertical levels.

2.3. Satellite Data

Satellite data were used to characterize the wind regime in the ESB and to map the mean Sea Surface Temperature (SST) signal of the coastal upwelling plume. Daily, 25 km resolution wind stress data were derived from the *Multiple-Satellite Blended Sea Surface Winds* product, made available by the National Oceanic and Atmospheric Administration (NOAA) [*Zhang et al*., 2006]. The 4 km resolution summer SST climatology (1982–2008) was derived from the Pathfinder Project (version 5.0) data, also made available by NOAA [*Casey et al*., 2010].

3. Numerical Models

3.1. Process-Oriented Experiments

In this study, we chose a process-oriented approach, in which the responses of the system to different forcing scenarios are diagnosed and compared. A set of semi-idealized numerical experiments was designed to investigate the individual and combined effects of bottom topography, wind forcing, and deep-ocean forcing. Here, deep-ocean forcing refers to the effects of the climatological BC jet. Specifically, we performed

Table 1. Outline of the Process-Oriented Numerical Experiments Performed With ROMS

Experiment	Initial/Boundary Conditions	Topography	Wind Forcing
EXP-smoo-1	Flat stratification	Smooth	Steady
EXP-smoo-2	Mean BC jet	Smooth	None
EXP-smoo-3	Mean BC jet	Smooth	Steady
EXP–real–1	Flat stratification	Rough	Steady
EXP–real–2	Mean BC jet	Rough	None
EXP–real–3	Mean BC jet	Rough	Steady

each experiment with different combinations of the following features: (1) either flat stratification (horizontal isopycnals) or BC stratification (tilted isopycnals); (2) either smooth (idealized) or rough (realistic) topography; and (3) either no wind forcing or steady wind forcing.

In this framework, we compared a BC-free scenario (flat stratification) with a scenario where the stratification is in thermal wind balance with an idealized BC jet (as described in the next section). The comparison of the model results in both scenarios provided insight on the role of the mean baroclinic signal of the BC, i.e., the intrinsic uplifting of isopycnals linked to the geostrophic shear of the current, and other effects related to the interaction of the BC flow with the continental shelf. Table 1 summarizes the set of process-oriented experiments performed.

Each experiment was run for 21 local inertial periods (one local inertial period ≈34 h), or ≈30 days. Instantaneous outputs were averaged over half an inertial period. In the following sections, the model fields described are time averages of the entire 30 day simulation, unless otherwise noted. The rationale for this choice is that experiments with the BC develop energetic instabilities along the continental slope, therefore introducing unwanted time-dependent features on the instantaneous fields. This effect was minimized by averaging over the first 30 days of the simulation. The choice of averaging over this amount of time was motivated by the fact that, in runs where the idealized BC is present, the shelf-averaged horizontal kinetic energy completes approximately two periods in 30 days (not shown). For consistency in the comparisons performed in the following sections, all runs were therefore averaged over 30 days. The fact that the 30 day averaged model fields in runs EXP-smoo-1,2,3 do not differ significantly from the fields averaged over the last 15 days (not shown) further supports the point that the 30 day averaged model fields are representative of both the fully developed wind-driven circulation and the mean BC jet.

3.2. Numerical and Parametric Modeling Setup

Our process-oriented experiments are implemented with the Regional Ocean Modeling System (ROMS) [*Shchepetkin and McWilliams*, 2005], which has already been successfully used for the ESB [e.g., *Soutelino et al*., 2013]. ROMS is a free-surface, terrain-following coordinate model that solves the primitive equations of motion under the Boussinesq and hydrostatic approximations.

The horizontal grid is rectangular (spanning the 41.6°W–36.1°W, 23.3°S–18.2°S longitude-latitude box) and has an average resolution of ≈930 m. The western boundary is closed and the eastern, southern, and northern boundaries are open. Different forms of radiation/nudging boundary conditions are used for the tracers and barotropic/baroclinic velocity components. Harmonic (i.e., Laplacian) lateral mixing is used for momentum and tracers. Momentum is mixed along S-surfaces and tracers are mixed along geopotential surfaces. A sponge layer with ≈15 grid points was used at the open boundaries, where the horizontal viscosity coefficient A_H was linearly ramped from its interior value of 10 $m^2\ s^{-1}$ to 100 $m^2\ s^{-1}$ at the open boundaries. The vertical viscosity coefficient A_V is found at each time step with the Mellor-Yamada level-2.5 turbulent closure scheme [e.g., *Wijesekera et al*., 2003]. Bottom stress was parameterized using a quadratic bottom drag law, with a canonical value of $C_D = 3\times10^{-3}$ for the bottom resistance coefficient.

The form of the vertical stretching curve was chosen such that the spacing of the 50 vertical S-levels was no coarser than 45 m. Bottom topography from an updated version of the *Smith and Sandwell* [1997] data set (SRTM30-plus) is used. The 30 arc second raw topography data were linearly interpolated to the model grid, and capped at 1200 m. The topography was then smoothed with a Hanning window.

The stretching curve, the number of vertical levels, the amount of smoothing applied, and the maximum model depth were chosen to bring the spurious velocities produced by the Horizontal Pressure Gradient Errors (HPGEs) to a tolerable level, while maintaining a reasonable computational cost and retaining desired morphological features. The optimal combination of grid parameters was that which minimized the quantities $\Delta h/h$ [*Beckmann and Haidvogel*, 1993] and $\Delta z/z$ [*Haney*, 1991]. These ratios quantify the hydrostatic

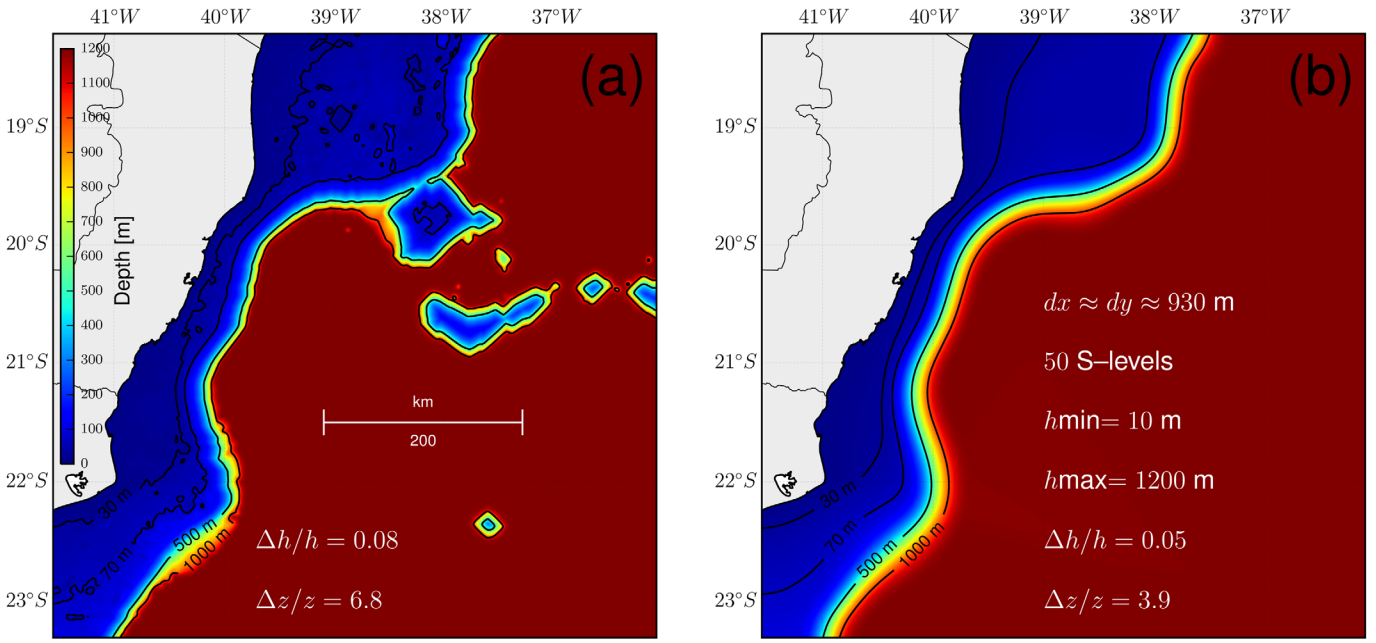

Figure 2. Bottom topographies used in the simplified model experiments. (a) Rough (realistic) topography grid. (b) Smooth (idealized) topography grid. Model grid details are shown, and are identical for both grids, except for the hydrostatic consistency ratios $\Delta h/h$ and $\Delta z/z$.

consistency of the grid, by means of the maximum steepness of the bottom topography and S-surfaces, respectively. $\Delta h/h \equiv (h_i - h_{i-1})/(h_i + h_{i-1})$, where h is the depth of a grid cell and i is an index in either horizontal direction. $\Delta z/z \equiv (z_{i,k} - z_{i-1,k} + z_{i,k-1} - z_{i-1,k-1})/(z_{i,k} + z_{i-1,k} - z_{i,k-1} - z_{i-1,k-1})$ is like a three-dimensional version of $\Delta h/h$. The final value of each of these parameters is the absolute maximum found after iterating over all grid cells in both horizontal directions.

The effects of the VTR and the smaller-scale topographic features on the continental shelf were examined using two separate grids, different only with respect to bottom topography. On the first grid (Figure 2a), the topography underwent the least possible smoothing, with the single purpose of decreasing the HPGEs. On the second grid (Figure 2b), the VTR was totally removed, and the topography was further smoothed to filter out the smaller-scale topographic features of the continental margin.

3.2.1. Flat-Stratification Initial Condition

In order to address the isolated response of the system to wind forcing, we must first study a BC-free scenario. The flat-stratification field used as initial condition for the BC-free experiments was derived from the WOA13 temperature and salinity fields. First, the summer climatological profiles shallower than 200 m were averaged together over the ESB (22°S–18°S), to produce a rough representation of the mean summer stratification on the continental shelf. Then, a rectangular area to the south of the VTR and away from the shelf edge was chosen to produce a second pair of spatially averaged T–S profiles, meant to represent the deep-ocean stratification. The distance to the shelf edge was chosen to be 10 first-mode baroclinic radii of deformation (L_d), with $L_d \approx 40$ km [*Houry et al.*, 1987]. This choice was meant to represent an ocean approximately at rest, where the stratification is not perturbed by the thermal wind signal of a western boundary current. The shallow and deep profiles were then merged smoothly and interpolated to the vertical model grid at all horizontal grid points.

3.2.2. Brazil Current Parameterization

The BC jet is parameterized using the Feature-Oriented Regional Modeling System (FORMS) [*Gangopadhyay and Robinson*, 2002] technique. In FORMS, the water mass and velocity structures of regional synoptic features (e.g., fronts or eddies) are parameterized analytically, using parameters that are based on observations of these features.

Within the FORMS framework, we chose the velocity-based backward approach [*Lozano et al.*, 1996; *Gangopadhyay and Robinson*, 2002]. This approach consists of parameterizing the velocity field of the

chosen synoptic feature, and then deriving the tracer fields from it. The BC jet structure was parameterized as a surface-intensified, isobath-following Gaussian jet, using the formulation of *Soutelino et al*. [2013]. The mass structure (i.e., the temperature and salinity fields) was then calculated from the velocity field assuming that the BC jet is in thermal wind balance with the density field. Details of this methodology are found in *Soutelino et al*. [2013].

The parameters chosen for the model BC jet are intended to represent the observed core velocity, volume transport, and geometry (width and vertical extent) of the BC within the ESB [e.g., *Miranda and Castro*, 1982; *Evans et al*., 1983; *Stramma et al*., 1990; *Rodrigues et al*., 2007; *Silveira et al*., 2008; *Arruda et al*., 2013]. The transport (core velocity) is -5.1 Sv (-50 cm s^{-1}). The Gaussian width (depth) of the jet is 80 km (150 m). In a separate set of experiments designed to address the response of the shelf circulation to the BC intensity, the core velocity varies from -20 cm s^{-1} to -70 cm s^{-1} in -5 cm s^{-1} steps.

Mass conservation is enforced by prescribing an outflow at the southern boundary that is equivalent to the inflow at the northern boundary, and no flow through the eastern boundary. The Intermediate Western Boundary Current jet, whose core lies typically at about 800 m [e.g., *Boebel et al*., 1999; *Legeais et al*., 2013] is not considered, under the assumption that it is not a relevant direct forcing of the intrusions of SACW onto the continental shelf.

3.2.3. Model Wind Forcing

The steady wind forcing employed in the numerical experiments was spatially uniform and upwelling-favorable (southwestward). The wind stress was linearly ramped to its full magnitude (0.072 N m^{-2}) over an inertial period. The magnitude of the wind forcing was chosen based on the mean summer (January–March) along-shelf component of the wind stress (τ^{sy}, parallel to the $\approx -40.5^\circ$ coastline tilt), averaged over the TB shelf area. The τ^{sy} series was derived from the time average of the 1988–2013 daily scatterometer data set, considering only upwelling-favorable (i.e., $\tau^{sy} < 0$) snapshots. The wind stress vector $\vec{\tau^s} = (\tau^{sx})\hat{x} + (\tau^{sy})\hat{y}$ was derived from the wind velocity vector $\vec{U} = (U^x)\hat{x} + (U^y)\hat{y}$ 10 m above the sea surface using the standard bulk formula $\vec{\tau} = \rho_a C_{Da} ||\vec{U}|| \vec{U}$, where $\rho_a = 1.226$ kg m^{-3} is the air density and $(\hat{x}, \hat{y})$ are the unit vectors in the cross-shelf and along-shelf directions, respectively. The drag coefficient C_{Da} was parameterized using the traditional formula from *Large and Pond* [1981], modified for low wind speeds according to *Trenberth et al*. [1990].

3.3. Realistic Experiment

As an independent source of comparison for the simplified process-oriented experiments, we complement the available observations with outputs from a regional, nested implementation of the Hybrid Coordinate Ocean Model (HYCOM), originally analyzed by *Arruda et al*. [2013]. First, a coarser (1°/4 horizontal resolution) parent simulation was run for the entire Atlantic Basin (65°S–60°N) from 1948 through 2009, initialized with climatological fields and forced with monthly means of atmospheric reanalysis fields. Next, a finer (1°/24 horizontal resolution) child simulation for the western South Atlantic region (54°W–32°W and 34°S–12°S) was run from 2004 through 2009, forced with the same atmospheric products as the parent simulation and with lateral boundary conditions derived from the parent simulation fields. For details, the reader is referred to *Arruda et al*. [2013].

4. South Atlantic Central Water Intrusion Pathways

In this section, we examine the pathways through which SACW may enter the ESB shelf. We begin with simple analyses of the hydrographic observations, and then seek more detailed evidence in the process-oriented and realistic numerical solutions.

4.1. Observational Setting

One of the striking features of the ESB is seasonal coastal upwelling. This process is relevant to the present study because it is well-known that the cold water that outcrops during coastal upwelling events has relatively higher SACW content. Therefore, investigating the surfacing of the thermocline in the ESB is likely to provide insight on the intrusion processes we are ultimately concerned with.

Satellite-derived SST images found in previous studies reveal a SST minimum on the shelf centered at ≈21°S, which is most intense during summer [e.g., *Mazzini and Barth*, 2013, their Figure 5]. The summer SST climatology derived from the Pathfinder v5.0 fields (Figure 3a) supports these observations, depicting a temperature minimum area (≈24.5°C) on the shelf originating at ≈19.5°S. This climatological coastal upwelling plume widens downstream, and reaches the shelf edge at ≈21°S.

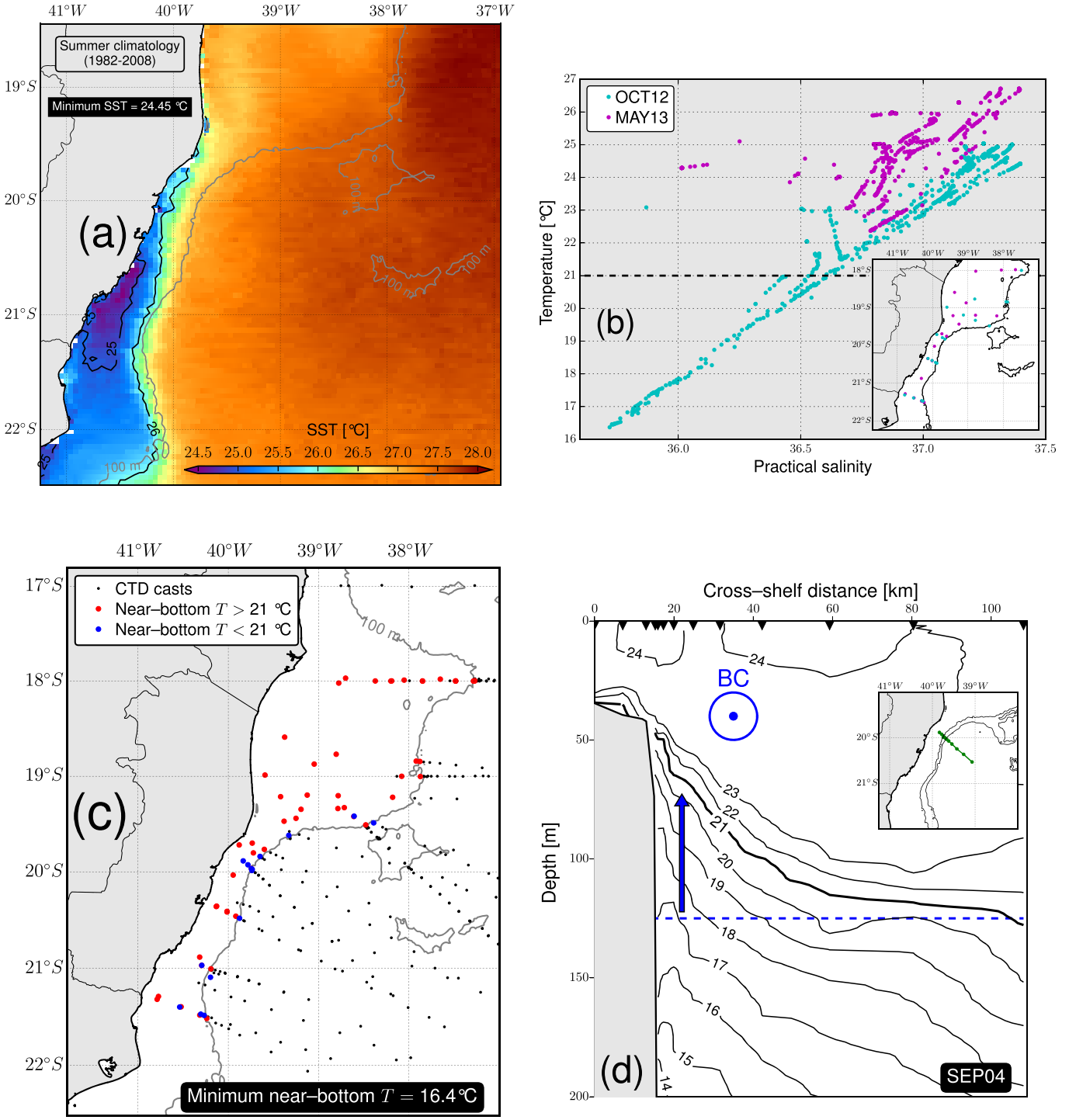

Figure 3. Hydrographic observations in the ESB shelf. (a) SST summer climatology. (b) Scattered *T–S* diagram for two contrasting hydrographic snapshots: Cyan (magenta) dots correspond to a scenario with (without) SACW on the shelf. (c) Near-bottom temperature map derived from all CTD casts of the five synoptic cruises. The black dots mark the locations of all CTD casts. The blue dots mark the casts shallower than 100 m where the near-bottom temperature was lower than 21°C (a qualitative evidence of water with high SACW content). (d) Cross-shelf temperature section from the SEP04 survey (September/2004) along a transect at the narrowest part of the shelf. The black triangles along the top of the figure mark the along-transect positions of the CTD casts. The green dots on the map insert mark the position of the CTD casts within the ESB. The blue-dashed line marks the approximate depth of the 21°C isotherm in a hypothetical scenario without the BC.

The wind regime is, on average, strongly upwelling-favorable. Considering the time series derived from the daily scatterometer data set, the along-shelf component of the wind stress vector τ^{sy} was upwelling-favorable 80% of the time in the period 1 January 2002 to 9 February 2013. This result highlights the likely

Table 2. Shelf-Averaged Buoyancy Frequency Squared (N^2), Slope Burger Number ($S \equiv \alpha N/f$), and its Square for the TB (19.5°S–22°S)

Survey	N^2 ($10^{-4}s^{-2}$)	α^2N^2/f^2	$\alpha N/f$
SEP04	1.03	0.22	0.46
MAR05	4.10	0.85	0.92
SEP07	0.49	0.10	0.32
OCT12	2.10	0.44	0.66
MAY13	1.16	0.24	0.49
Average	**1.78**	**0.37**	**0.57**

major importance of the wind forcing. A similar conclusion was reached for the Cape São Tomé area (22°S), where τ^{sy} was upwelling-favorable 78% of the time between 2000 and 2011 [*Palóczy et al*., 2014].

The question of how the SACW gets to the coast before outcropping then arises. Does it penetrate on the shelf locally or upstream (north) of the SST minimum? As a first attempt to address this question, a simple analysis of the near-bottom temperature was done, as the cold SACW signal is observed mostly in the lower half of the water column, and is bottom intensified. Figure 3c shows a map of near-bottom temperature, indicating stations where SACW was observed. Based on the knowledge that during upwelling events in the ESB the average SST is ≈21°C [*Castro et al*., 2006], this isotherm was chosen as a tracer for SACW. In four of the five synoptic cruises analyzed, SACW was observed in at least one of the stations shallower than 100 m of every transect occupied between 19.5°S and 21.5°S. The only exception was the MAY13 survey, when no water colder than 22.3°C was observed inshore of the 100 m isobath (Figure 3b). In the surveys analyzed, SACW was not observed north of 19.25°S (Figure 3c). The lowest temperature measured on the shelf was 16.4°C, around the 50 m isobath at the southernmost transect of the OCT12 survey. Evidently, this result does not mean that SACW never enters the shelf north of 19.25°S. Rather, it suggests that intrusion events tend to be more common to the south of the VTR, all along the TB and the southern flank of the wide AB.

The scattered Temperature-Salinity (T–S) diagram in Figure 3b highlights the typical water mass structure on the ESB shelf. Warm and salty TW in the mixed layer interfaces with cold and fresh SACW advected onshore from the oceanic pycnocline, with little evidence of a modified (fresher) coastal water mass. This stresses the point made in the previous paragraph, as the water with highest SACW content (coldest and freshest) is observed to the south of the VTR rather than to the north of it.

The cross-shelf structure of the temperature field in the ESB (Figure 3d) reveals the well-known presence of the BC jet. The thermocline and the pycnocline are uplifted near the shelf edge, and a layer of relatively cold, fresh, and dense water occupies the shelf. There is a variety of physical mechanisms related to the BC that may play a role in the intrusions of SACW. Perhaps the simplest of those is the fact that colder branches of SACW are available at the shelf edge simply due to the presence of the BC there. It will be argued that this uplifting of the main thermocline is a key mechanism in setting the properties of the upwelling source water, as previously pointed out for nearby upwelling systems, namely the Cape São Tomé (22°S) [*Palóczy et al*., 2014] and Cape Frio (23°S) [*Cerda and Castro*, 2014] areas.

4.1.1. Buoyancy Arrest and Frictional Spin-Down Predictions

If along-shelf scales are much larger than cross-shelf scales, the nature of the response of the shelf circulation to low-frequency wind forcing is expected to be dominated by the barotropic mode when the quantity $S^2 = \alpha^2N^2/f^2$ (where α, N, and f are representative values for the bottom slope, buoyancy frequency, and Coriolis parameter, respectively) is small [*Clarke and Brink*, 1985]. Furthermore, fluctuations in the wind-driven flow at the shelf edge are expected to be negligible compared to fluctuations near the coast when $S = \alpha N/f$ is small, meaning that the entire wind-driven flow is trapped within the shelf and has little effect on the circulation in the shelf edge area [*Clarke and Brink*, 1985]. It is therefore insightful to estimate S from the CTD data.

Table 2 shows shelf-averaged (stations shallower than 100 m) values for each of the five surveys within the TB. The average bottom slope in the TB is $\alpha = 2.3\times10^{-3}$, and a reference absolute value for the Coriolis parameter is $f = 5.1\times10^{-5}$ s^{-1}. S^2 varied between 0.10 and 0.85, and S between 0.32 and 0.92. This implies that a significant baroclinic response is predicted throughout the shelf, and that the low-frequency wind-driven circulation at the shelf edge is expected to have a nonnegligible amplitude. This picture stands in contrast with regions where S^2 is much smaller and the shelf response is quasi-barotropic, such as the wintertime South Brazil Bight ($S^2 = 1.6\times10^{-4} - 1.9\times10^{-2}$) [*Stech and Lorenzzetti*, 1992], the São Paulo Continental Shelf ($S^2 = 2.2\times10^{-4}$ – 3.0×10^{-4}) [*Dottori and Castro*, 2009], or the wintertime West Florida Shelf ($S^2 = 5.0\times10^{-5}$) [*Clarke and Brink*, 1985]. The response to low-frequency wind forcing in the TB shelf is not expected, however, to be as baroclinic as in regions similar to the Peruvian shelf ($S^2 = 1.10 - 2.25$) [*Clarke and Brink*, 1985; *Lentz and Chapman*, 2004].

Buoyancy arrest also depends on S. In a stratified, sloping bottom Ekman layer, cross-shelf buoyancy advection produces a horizontal density gradient, which brings the near-bottom along-shelf velocity (hence along-shelf bottom stress) to rest through thermal wind shear. The absence of bottom stress implies no bottom Ekman transport. This mechanism is known as buoyancy arrest [e.g., *Garrett et al*., 1993; *Brink and Lentz*, 2010]. A rough estimate of the timescale T_{buoyancy} over which this phenomenon is expected to occur is given by the quantity $(S^2 f)^{-1}$ [*Garrett et al*., 1993]. For the five data sets considered here, T_{buoyancy} varies from 55 to 7 h, with a mean value of 15 h. This suggests that buoyancy arrest is more effective during stronger SACW intrusion events, when the shelf-averaged N^2 is higher, causing T_{buoyancy} to be shorter. However, a more thorough examination of the potential importance of buoyancy arrest would have to account for its along-shelf scale [*Brink*, 2012].

Alternatively, the wind-driven flow may simply undergo frictional adjustment before buoyancy arrest takes place. A first estimate of the frictional adjustment timescale T_{friction} is given by the quantity H/r [e.g., *Brink*, 1998], where H is the local depth and r is a linear bottom resistance coefficient. Assuming a canonical value of 3×10^{-4} m s^{-1} for r, T_{friction} is 65 h at the 70 m isobath, and 19 h at the 20 m isobath. Compared to the 7–55 h estimated range for T_{buoyancy}, it seems that a combination of buoyancy and friction-induced adjustment of the flow should be expected, with the buoyancy effects possibly being more important during stronger SACW intrusion events. For comparison, typical velocity adjustment timescales found in the model results just inshore of the 70 m isobath within the TB (i.e., the approximately straight part of the shelf) are 2–3 days.

4.2. Model Kinematics of SACW Intrusions

While the synoptic observations discussed in the previous section yield some insight on the SACW intrusions, a more detailed examination of the pathways and physical mechanisms involved require a numerical approach. We start by looking at the passive tracer (dye) fields from the process-oriented numerical experiments.

4.2.1. Passive Tracer Distributions

The dye fields were initialized by setting the dye concentration (in kg m^{-3}) to be numerically equal to the local depth (in meters) at each grid point. Figure 4 presents snapshots of horizontal distributions of the fractional thickness of the layer occupied by water initially offshore of the 70 m isobath (approximately the shelfbreak depth). In other words, it shows the thickness of the layer occupied by water with dye concentration equal to or greater than 70, divided by the local depth.

Figure 4 shows that slope water penetrates the model shelf mostly within the TB. While this does not imply that the TB shelf is the only possible slope water intrusion location, the agreement with the observations (see bottom temperature map, Figure 3c) suggests that it is the most frequent. This intrusion area is active under all forcing scenarios (wind-only, BC–only, and wind+BC), although clearly only wind forcing is capable of driving slope water all the way to the inner shelf. The rough topography scenarios show more irregular distributions, similar to their smooth topography counterparts only with respect to the overall intrusion locations at the shelf edge. There seems to be a weaker intrusion spot on the southern flank of the AB, which is more evident in the wind-driven rough topography scenarios (Figures 4b and 4d). This suggests that some kind of local mean flow-topography interaction process could be relevant there, in addition to the tidal flow-topography interaction mechanisms suggested by *Pereira et al*. [2005]. For simplicity, we discuss only the smooth topography experiments in the following sections.

Unlike the wind-driven intrusions, the BC-driven intrusions occupy the entire water column around the shelf edge area, and are therefore likely to cause TW to penetrate the outer shelf along with SACW in certain parts of the TB. This point is demonstrated by the slope water layer thickness distributions in the BC–only scenarios, which are equal to the local depth near the shelfbreak (Figures 4e and 4f). In contrast, the wind-driven experiments show bottom-intensified SACW intrusions that reach farther onshore on the TB shelf, followed by a top-bottom slope water layer within the coastal upwelling plume (Figures 4a–4d).

4.2.2. Velocity and Temperature Distributions

The surface and near-bottom temperature and velocity distributions from EXP-smoo-1 (wind-only) and EXP-smoo-3 (wind+BC) are shown in Figures 5a–5d. The main difference is that EXP-smoo-3 produces colder SACW intrusions (≈1°C colder), that penetrate farther inshore at the three areas indicated in Figures 5b and 5d. Both EXP-smoo-1 and EXP-smoo-3 realistically reproduce the shape of the coastal upwelling plume, compared to the observed climatological SST pattern (Figure 3a).

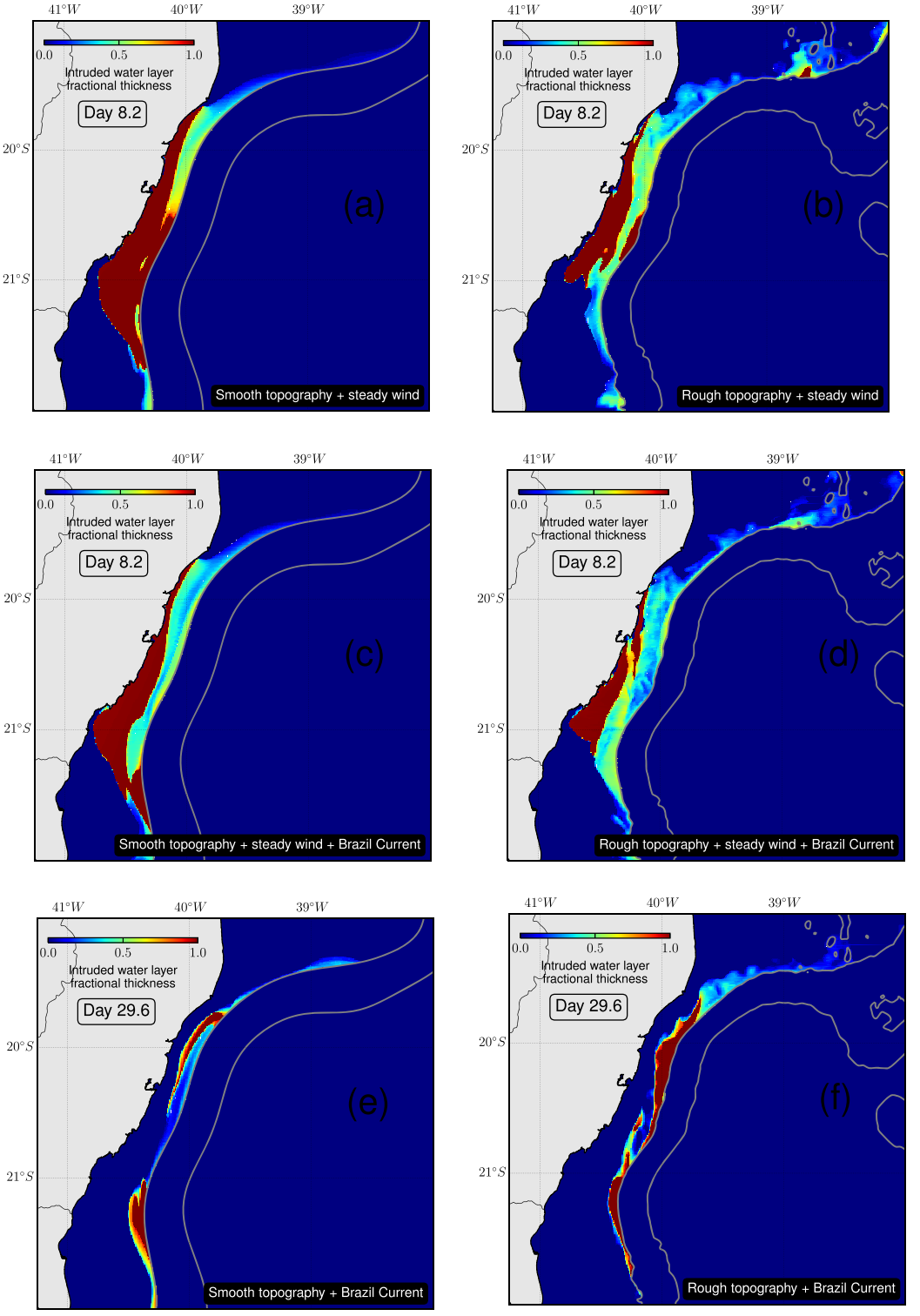

Figure 4. Instantaneous maps of the thickness of the layer occupied by intruded water on the shelf normalized by the local depth. In red areas, the entire water column is occupied by water that was located offshore of the 70 m isobath (approximately the shelfbreak depth) in the initial conditions. In blue areas, no water originally offshore of the shelfbreak is present. (a, c, e) Smooth topography experiments. (b, d, f) Rough topography experiments. (a, b) Wind–only experiments. (c, d) Wind + BC experiments. (e, f) BC–only experiments. In the wind-forced experiments (a–d), the instantaneous fields are shown for model day 8.2, at the end of the spin-up of the shelf circulation. In the BC–only experiments (e, f), the instantaneous fields are shown for the last model day (29.6). The thick gray lines represent the 70 and 1000 m isobaths.

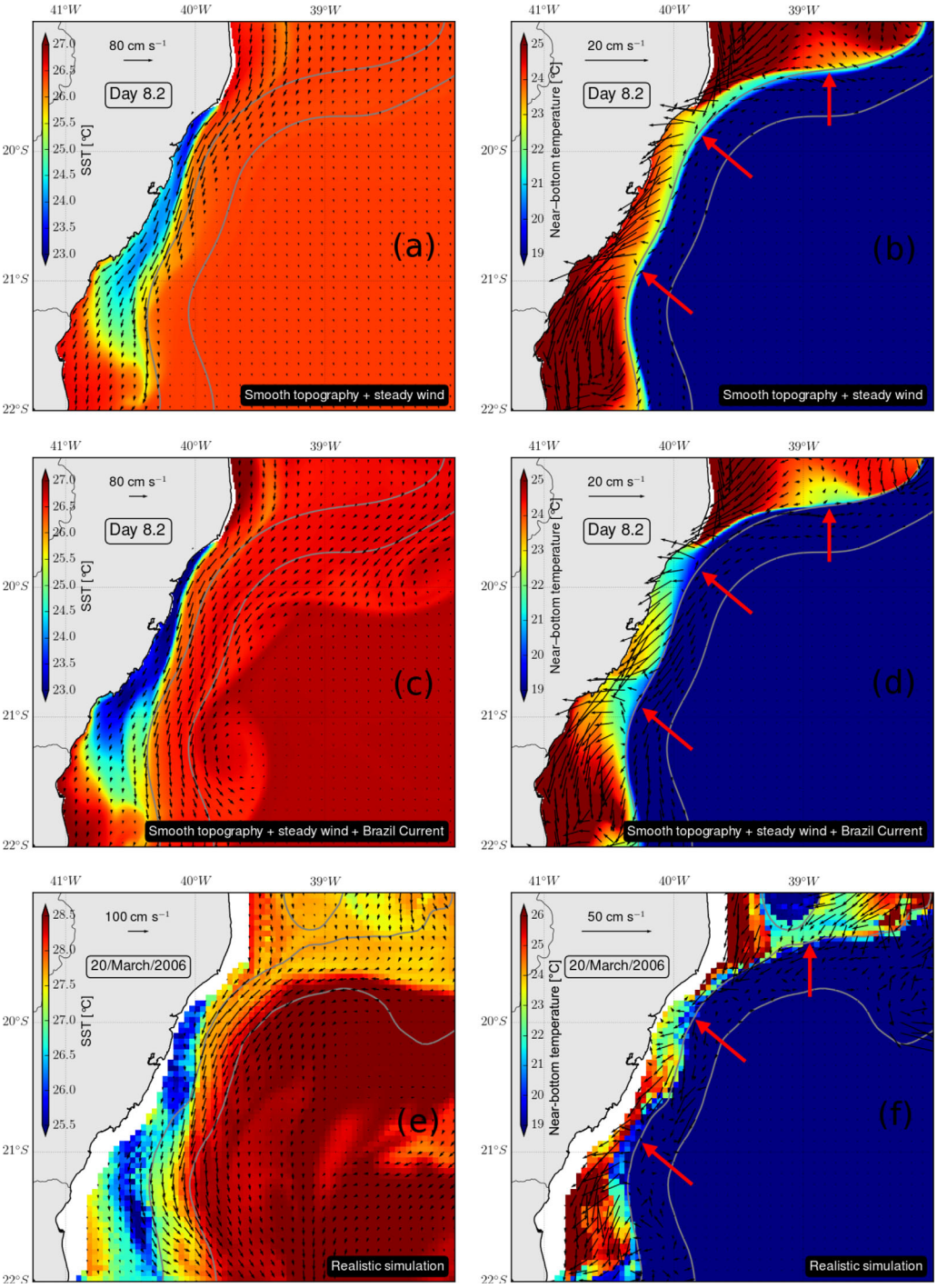

Figure 5. Instantaneous temperature (color shading) and velocity (vectors) at the surface and near the bottom. (a, b) EXP-smoo-1 simplified experiment (wind–only). (c, d) EXP-smoo-3 simplified experiment (wind+BC). (e, f) Realistic experiment. (a, c, e) Temperature and velocity at the surface. (b, d, f) Temperature and velocity near the bottom. The red arrows in the right column plots indicate preferential areas of onshore flow. The gray lines mark the 70 and 1000 m isobaths. For clarity, every tenth (second) vector is drawn in the upper and middle rows (bottom row).

The near-bottom temperature and velocity distributions from the process-oriented ROMS experiments reveal two major pathways of SACW intrusion within the TB and one in the southern flank of the AB (Figures 5b and 5d). The realistic HYCOM simulation has a coarser horizontal resolution (≈4.5 km) than the process-oriented experiments, and therefore is not expected to represent the coastal circulation as well as the deep-ocean circulation (details on the model verification are found in *Arruda et al.* [2013]). Despite this

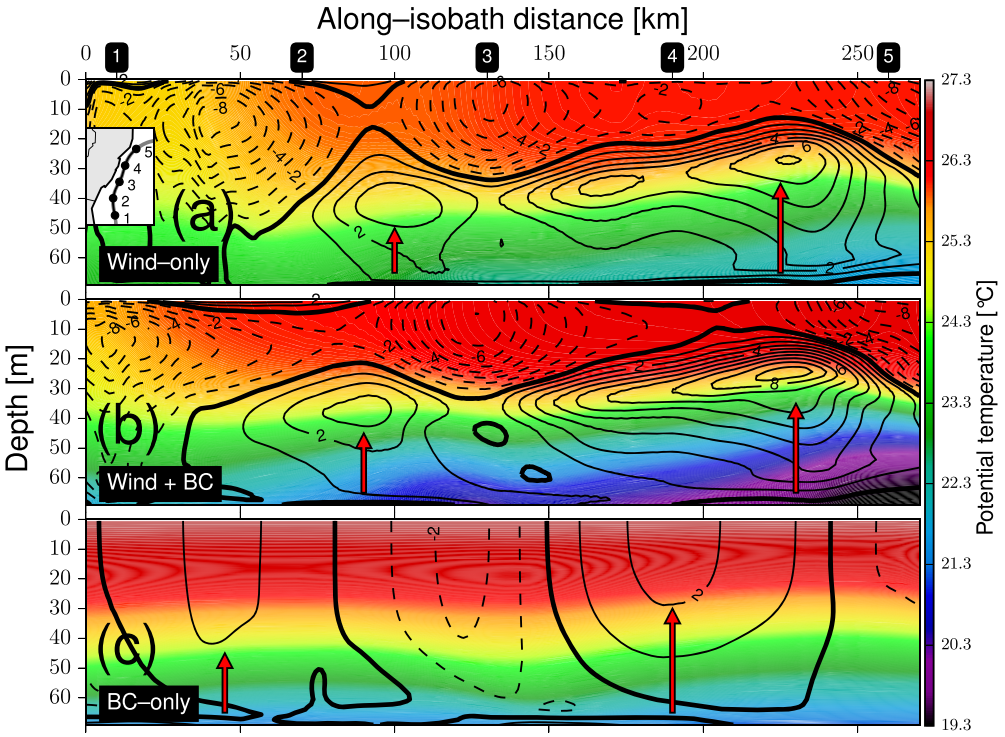

Figure 6. Run-averaged (30 days) potential temperature (color shading) and cross-isobath velocity in cm s^{-1} (black contours) distribution along the 70 m isobath for the smooth topography scenarios. Solid (dashed) contours represent onshore (offshore) velocity. The heavy black line is the zero contour. (a) EXP-smoo-1 (wind–only). (b) EXP-smoo-3 (wind+BC). (c) EXP-smoo-2 (BC–only). The red arrows indicate preferential pathways of onshore flow of cold SACW. The markers labelled 1–5 along the *x* axis of the top plot correspond to the dots on the 70 m contour of the map insert, which also shows the Brazilian coastal land mass (shaded).

limitation, some snapshots from the realistic simulation do represent similar intrusion pathways (Figure 5f shows an example).

The model temperature and cross-isobath velocity vertical structures along the TB shelfbreak are consistent with the dye distributions, in that the onshore flow occupies the lower half of the water column in the wind-driven scenarios, but spreads throughout the water column and is surface-intensified in EXP-smoo-2 (BC–only, Figures 6 and 7). The maximum onshore velocity is ≈9 cm s^{-1} and ≈7 cm s^{-1} in EXP-smoo-3 and EXP-smoo-1, respectively, but only ≈2 cm s^{-1} in EXP-smoo-2. In both wind-driven scenarios, the maximum onshore velocity is not found near the bottom, as classic, homogeneous Ekman Theory predicts. Rather, it is found at middepth (≈30–40 m), consistent with the theoretical predictions of *Lentz and Chapman* [2004] for $S \equiv \alpha N/f$ close to unity ($S \approx 1$ in the estimates for the most strongly stratified cases observed in the TB, see Table 2). According to these authors, this middepth intensification of onshore flow is linked to the divergence of nonlinear cross-isobath momentum advection. Besides this mechanism, local acceleration or an along-isobath pressure gradient force can also produce onshore return flow.

The maximum onshore velocity is located at the narrowest part of the shelf in both wind-driven experiments (between along-shelf locations 4 and 5, see Figures 6a and 6b). At this location, the thermocline reaches its minimum depth and water as cold as 22°C and 19.5°C is found at the bottom in EXP-smoo-1 (wind-only) and EXP-smoo-3 (wind+BC), respectively. This difference in bottom temperature highlights the effect of the BC in modifying the upwelling source water temperature, causing colder branches of SACW to enter the shelf.

Another point worth stressing is the qualitative similarity between the sections of the cross-isobath velocity component in both wind-driven experiments (Figure 6). The EXP-smoo-3 (wind+BC) section is very similar to the sum of the EXP-smoo-1 (wind-only) and EXP-smoo-2 (BC–only) sections. In fact, the normalized root mean square difference between the EXP-smoo-3 section and the sum of EXP-smoo-1 and EXP-smoo-2 sections is only 7.8%. This indicates that, at the shelfbreak, the total model cross-isobath circulation is almost a linear superposition of the individual effects of the wind and BC forcings.

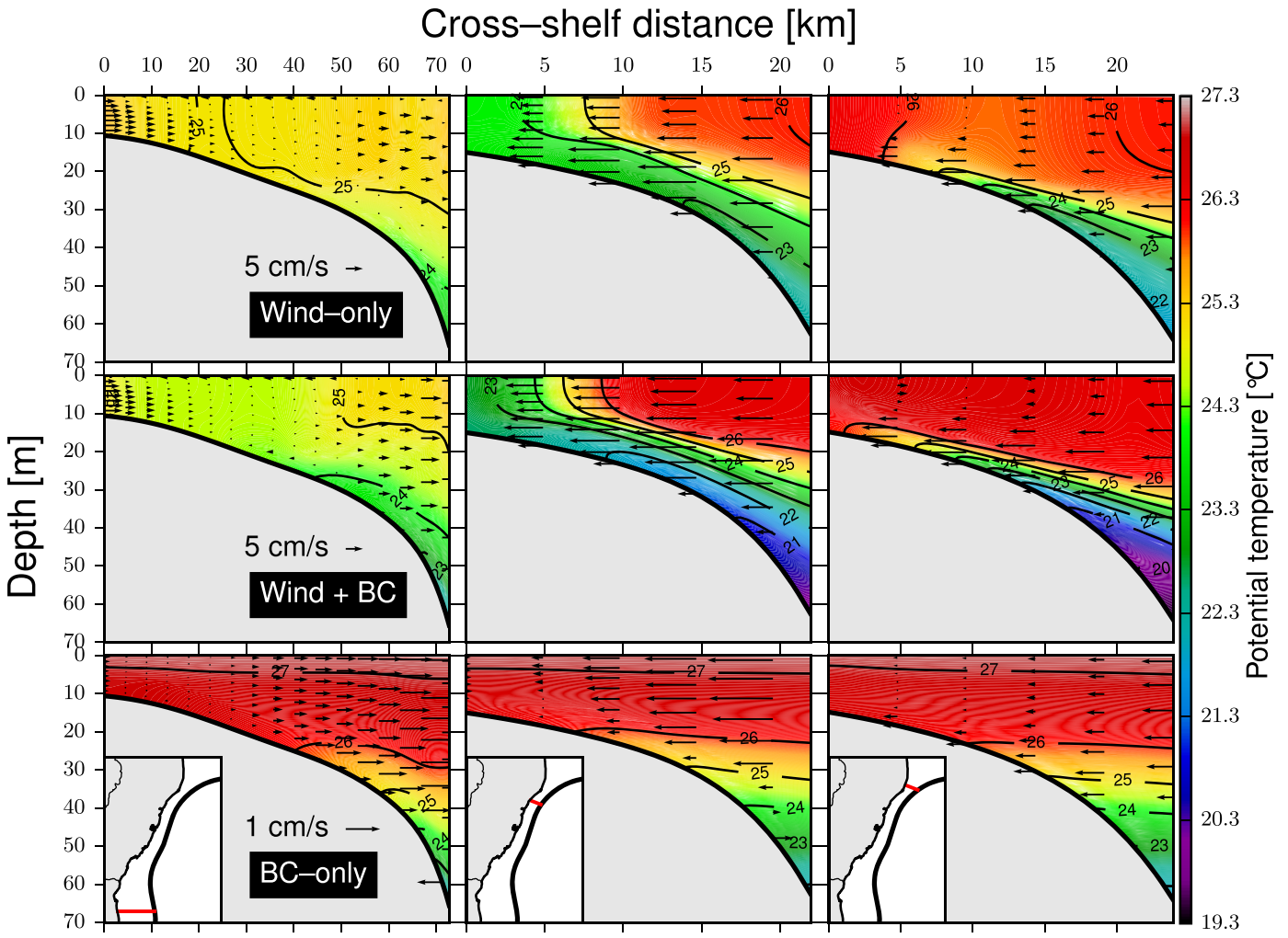

Figure 7. Run-averaged (30 days) potential temperature and cross-isobath velocity (black arrows) along three cross-shelf transects for the smooth topography experiments. (top plots) EXP-smoo-1 (wind–only). (middle plots) EXP-smoo-3 (wind+BC). (bottom plots): EXP-smoo-2 (BC–only). The left, middle, and right columns each correspond to a different cross-shelf location, marked as a red line on the map inserts on the bottom plot of each column. The reference cross-shelf velocity vectors for each experiment are shown in the left-column plots. Note that the scales in the velocity vectors and in the *x* axis are different.

The cross-shelf temperature distributions further stress the depth-dependent character of the SACW intrusions within the TB. For both wind-driven scenarios, the three cross-shelf transects in Figure 7 show different regimes. The southernmost transect reflects the well-mixed character of the shelf and the offshore displacement of the coastal upwelling plume all the way to the shelf edge. The middle transect is located at the narrowest part of the shelf, where the maximum onshore velocity is found, and where the thermocline is shallowest. In this area, a mature coastal upwelling front is found ≈5–10 km away from the coast. The northernmost transect reveals a clear bottom-trapped temperature front, but no coastal upwelling plume. The intrusions in EXP-smoo-2 (BC–only) are also consistent with the interpretation suggested by the dye distributions. SACW does not reach the surface, and the uplift of the isotherms in the bottom-trapped temperature front is much gentler than in the wind-driven scenarios (Figure 7, bottom plots).

5. Along-Isobath Momentum Balance

At this point we have presented evidence that SACW tends to enter the ESB shelf at preferential along-shelf locations. But what are the physical mechanisms involved? We begin to address this question by examining the momentum budget in the process-oriented numerical solutions.

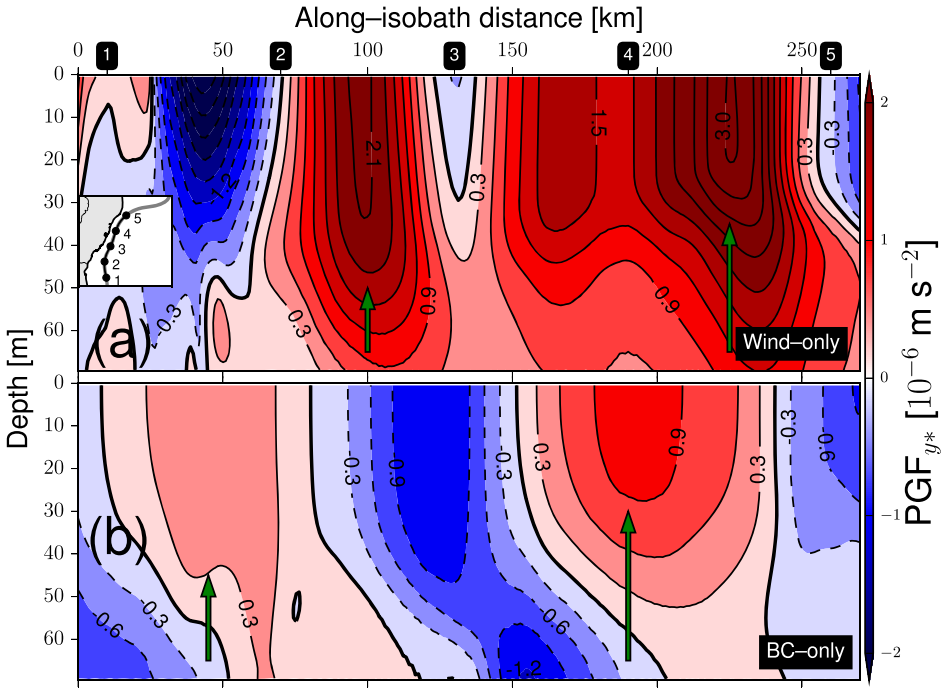

Figure 8. Run-averaged (30 days) along-isobath pressure gradient force (PGF$_{y*}$) along the 70 m isobath for the smooth topography scenarios. (a) EXP-smoo-1 (wind–only). (b) EXP-smoo-2 (BC–only). The heavy black line is the zero contour. The green arrows indicate preferential pathways of onshore flow, as in Figure 6. The markers labeled 1–5 along the *x* axis of the top plot correspond to the dots on the 70 m contour of the map insert, which also shows the Brazilian coastal land mass (shaded).

5.1. Depth-Dependent Momentum Balance Along the Shelf Edge

In this section, we write the momentum equations in an isobath-following coordinate system, using the procedure described in *Gan et al.* [2009]. In this new coordinate system, $\hat{y}^*$ ($\hat{x}^*$) is the along-isobath (cross-isobath) direction. $\hat{y}^*$ ($\hat{x}^*$) is positive equatorward (offshore). The rationale for using this transformed framework of reference is that it is a more convenient approach to the study of flows that deviate from geostrophy and transport mass across isobaths, breaking the Taylor-Proudman constraint. The along-isobath component of the momentum budget, with pressure in kinematic units (i.e., divided by the Boussinesq reference density $\rho_0 = 1025$ kg m^{-3}) is

$$\underbrace{\frac{\partial v}{\partial t}}_{\mathrm{ACCEL}_{y*}} \underbrace{+u\frac{\partial v}{\partial x*}+v\frac{\partial v}{\partial y*}+w\frac{\partial v}{\partial z}}_{\mathrm{NL}_{y*}} \underbrace{+fu}_{\mathrm{COR}_{y*}} = \underbrace{-\frac{\partial p}{\partial y*}}_{\mathrm{PGF}_{y*}} \underbrace{+\frac{\partial}{\partial z}\left(A_V\frac{\partial v}{\partial z}\right)}_{\mathrm{VVIS}_{y*}} \underbrace{+A_H\left(\frac{\partial^2 v}{\partial x*^2}+\frac{\partial^2 v}{\partial y*^2}\right)}_{\mathrm{HVIS}_{y*}}, \quad (1)$$

where u, v, and w are the cross-isobath, along-isobath, and vertical velocity components, respectively, f is the local inertial frequency, p is pressure, and A_V (A_H) is the vertical (horizontal) turbulent viscosity coefficient. $\mathrm{PGF}_{y*} \equiv \frac{g}{\rho_0}\int_\eta^z \frac{\partial \rho}{\partial y*}dz' - g\frac{\partial \eta}{\partial y*}$ is the total along-isobath pressure gradient force per unit mass, with g being the acceleration due to gravity, ρ the total density, and η the free-surface displacement. The along-isobath momentum balance relates directly to the cross-isobath circulation, and geostrophy was found to dominate the cross-isobath momentum balance in all experiments, as consistently supported by observational evidence for the subtidal mean flow on most continental shelves [e.g., *Lentz and Chapman*, 2004, and references therein]. For these reasons, only the along-isobath momentum balance is discussed here. In addition, due to the similarity between the wind+BC experiment (EXP-smoo-3) and the wind-only experiment (EXP-smoo-1), we restrict ourselves to comparing results from the wind-only (EXP-smoo-1) and BC–only (EXP-smoo-2) experiments.

Along the 70 m isobath (approximately the shelfbreak depth), there are areas where PGF$_{y*}$ is positive (i.e., equatorward, Figure 8). Part of this equatorward PGF$_{y*}$ gives rise to a geostrophically balanced onshore flow, which has been found to be an important source of onshore transport in many continental shelves [e.g., *Scott and Csanady*, 1976; *Palma and Matano*, 2009; *Pringle and Dever*, 2009; *Gan et al.*, 2009, 2013; *Xu*

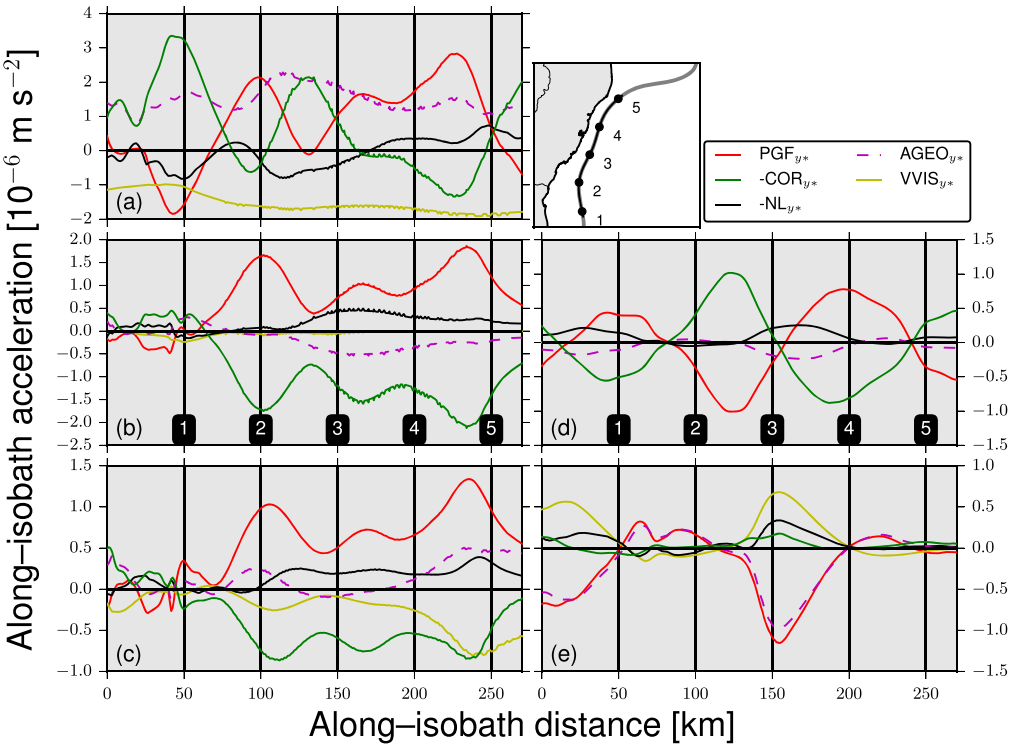

Figure 9. Run-averaged (30 days) and layer-averaged momentum balance terms in the along-isobath direction along the shelf edge (70 m isobath). (a–c) EXP-smoo-1 (wind–only). (d, e) EXP-smoo-2 (BC–only). (a) Surface Ekman layer average. (c, e) Bottom Ekman layer average. (b, d) Geostrophic interior average. The term $\mathrm{AGEO}_{y*} \equiv -\frac{\partial p}{\partial y*} - fu$ is the ageostrophic along-isobath pressure gradient force. The vertical lines labeled 1–5 correspond to the dots on the 70 m contour of the map insert, which also shows the Brazilian coastal land mass (shaded).

et al., 2015; *McCabe et al.*, 2015], but that had not yet been examined and quantified in the ESB. The PGF_{y*} is surface-intensified in both EXP-smoo-1 (wind-only) and EXP-smoo-2 (BC–only), and tends to not change sign vertically. The EXP-smoo-2 scenario features a more clearly periodic pattern, with alternating areas of equatorward PGF_{y*} (onshore geostrophic flow) and poleward PGF_{y*} (offshore geostrophic flow). Finally, the amplitude of the PGF_{y*} in EXP-smoo-1 is greater than the amplitude of the PGF_{y*} in EXP-smoo-2 by a factor of ≈3. This ratio is similar to the ratio between onshore velocities across the shelfbreak (Figures 6a and 6c).

The spatial patterns of the individual momentum advection terms ($u\frac{\partial v}{\partial x*}$, $v\frac{\partial v}{\partial y*}$, and $w\frac{\partial v}{\partial z}$) are qualitatively similar and nearly balance each other (not shown), leaving a net momentum advection NL_{y*} of $O(10^{-6})$ m s^{-2} or smaller. In all experiments, the local acceleration (ACCEL_{y*}) and horizontal viscosity terms (HVIS_{y*}) are everywhere $O(10^{-7})$ m s^{-2} or smaller (not shown), which is at least one order of magnitude smaller than the next-largest terms. Therefore, we exclude ACCEL_{y*} and HVIS_{y*} of all analyses for simplicity.

To close the momentum budget, it is helpful to examine the vertical structure of the terms in equation (1) and the part of the PGF_{y*} that is left unbalanced by the Coriolis acceleration, i.e., $\mathrm{AGEO}_{y*} \equiv -\frac{\partial p}{\partial y*} - fu$. Figure 9 presents the vertically averaged terms within the surface Ekman layer (0–40 m), the geostrophic interior (40–60 m) and the bottom Ekman layer (60–70 m). The thickness of the Ekman layers was defined based on the vertical structure of the vertical friction term (VVIS_{y*}, not shown).

Within the geostrophic interior, the ageostrophic pressure gradient force AGEO_{y*} is approximately balanced by net nonlinear momentum advection NL_{y*} in both the wind and BC-forced cases (Figures 9b and 9d). Therefore, away from the Ekman layers, the simplified momentum balance is

$$fu \approx -\frac{\partial p}{\partial y^*} - \mathrm{NL}_{y*}, \tag{2}$$

Considering the wind-driven case, the combination of this result with the middepth position of the maximum onshore return flow (Figure 6a) alludes to the dynamical regime predicted by *Lentz and*

Chapman [2004] under strong stratification. Within the surface and bottom Ekman layers in the wind-driven case, $AGEO_{y*}$ is approximately balanced by the vertical viscosity $VVIS_{y*}$, and to a lesser extent, momentum advection NL_{y*} in the wind-only scenario (Figures 9a and 9c). The simplified momentum balance within the Ekman layers is then

$$fu \approx -\frac{\partial p}{\partial y^*} + \frac{\partial}{\partial z}\left(A_V \frac{\partial v}{\partial z}\right), \tag{3}$$

This leading-order balance has been found in other studies [e.g., *Palma et al*., 2008; *Palma and Matano*, 2009] within the bottom Ekman layer. It is interesting to note that the bottom Ekman layer in the BC–only case has a different balance (Figure 9e), with relatively smaller Coriolis acceleration COR_{y*} (consistent with the very small near-bottom cross-isobath velocities, Figure 6c).

The picture that emerges from this model analysis is that of an energetic cross-isobath circulation at the shelf edge, consistent with the predictions of *Clarke and Brink* [1985] for the observed values of the slope Burger number (Table 2). The PGF_{y*} drives a geostrophic onshore flow, and next-order effects related to momentum advection and friction seem to be important in different parts of the water column.

5.2. Depth-Averaged Momentum Balance

A question now worth examining is what dynamics dominates the cross-isobath circulation in a depth-averaged sense. We address this by evaluating the depth-averaged momentum budget. Neglecting the highest-order terms (local acceleration and horizontal viscosity), the depth-averaged momentum equation in the along-isobath direction is [e.g., *Warner et al*., 2014], with pressure and stresses in kinematic units (i.e., divided by the Boussinesq reference density $\rho_0 = 1025$ kg m^{-3}):

$$0 = \underbrace{\underbrace{-\frac{\partial (UV)}{\partial x*} - \frac{\partial (VV)}{\partial y*}}_{-\overline{NL_{y*}}} \quad \underbrace{-fU}_{-COR_{y*}} \quad \underbrace{-P_{y*}}_{\overline{PGF_{y*}}} \quad \underbrace{+\frac{\tau^{sy*}}{H}}_{SSTR_{y*}} \quad \underbrace{-\frac{\tau^{by*}}{H}}_{BSTR_{y*}}}_{} \tag{4}$$

where $(U, V) \equiv \frac{1}{H}\int_{-H}^{\eta}(u, v)\, dz$ are the depth-averaged velocity components in the cross-isobath and along-isobath directions, respectively, τ^{sy*} (τ^{by*}) is the surface (bottom) stress, H is the local depth, and $\overline{PGF_{y*}} \equiv \left(\frac{g}{H\rho_0}\int_{\eta}^{-H}\int_{\eta}^{z}\frac{\partial \rho}{\partial y*}dz'\, dz - g\frac{\partial \eta}{\partial y*}\right)$ is the depth-averaged total pressure gradient force per unit mass in the along-isobath direction. We point out that equations (1) and (4) do not include curvature effects, which are addressed in section 6.2.

5.2.1. Along-Shelfbreak Patterns

Figure 10 shows the along-shelfbreak distribution of the terms in equation (4) for two of the process-oriented experiments. It can be seen that there are areas of onshore flow (blue-shaded areas around point 2 and between points 3 and 5), and that the leading-order balance in EXP-smoo-1 (wind-only) is between the wind stress, the pressure gradient force and the Coriolis acceleration. In EXP-smoo-2 (BC–only), the water column is approximately in geostrophic balance. In both cases, momentum advection is the next-largest term, and bottom stress is the smallest of the terms considered. The ratio τ^{by*}/τ^{sy*} in the wind-only experiment is 0.12 or smaller, indicating that, along the shelfbreak, the offshore transport in the surface Ekman layer is ≈10 times larger than the onshore transport in the bottom Ekman layer.

The most general scenario (EXP-smoo-3, wind and BC forcings, not shown) is essentially a linear superposition of EXP-smoo-1 and EXP-smoo-2, in that the leading-order depth-averaged balance is between the pressure gradient force, the Coriolis acceleration, the wind stress, and net momentum advection. Simplifying equation (4) using this result, and multiplying it through by H/f yields

$$UH = \frac{\tau^{sy*}}{f} - \frac{H}{f}P_{y*} - \frac{H}{f}\overline{NL_{y*}}. \tag{5}$$

This can be seen as a form of the parallel transport model [*Csanady*, 1982]. The physical content of equation (5) is that the net cross-isobath volume transport per unit length (in the along-isobath direction) is a balance between offshore surface Ekman transport and onshore geostrophic transport induced by the equatorward PGF_{y*} throughout the water column (with a smaller contribution from momentum advection). This depth-averaged analysis confirms that the leading-order balance has a geostrophic component in all three forcing scenarios, especially in the BC–only case (EXP-smoo-2, Figure 10b). Moreover, the previous conjectures on

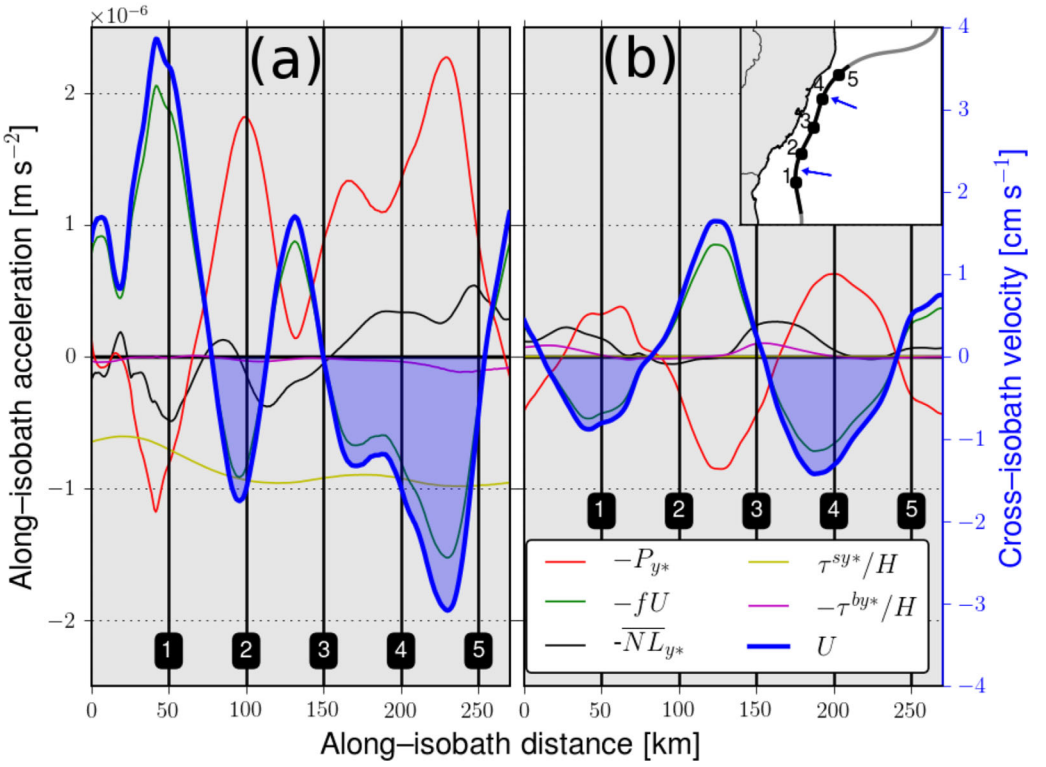

Figure 10. Run-averaged (30 days) and depth-averaged momentum balance terms in the along-isobath direction along the 70 m isobath for the process-oriented experiments. (a) EXP-smoo-1 (wind–only). (b) EXP-smoo-2 (BC–only). The blue-shading marks areas of onshore flow ($U < 0$), which are indicated by the blue arrows on the map insert. The vertical lines labeled 1–5 correspond to the dots on the 70 m contour of the map insert, which also shows the Brazilian coastal land mass (shaded).

the importance of the model nonlinear cross-isobath momentum advection [*Lentz and Chapman*, 2004] are supported.

The realistic HYCOM simulation reveals encouraging similarities with the simplified ROMS experiments. Specifically, the time-mean, depth-averaged flow across the shelfbreak is partly in geostrophic balance, and is onshore at the same preferential intrusion locations suggested by the results presented previously (blue-shaded areas in Figure 11). In the areas where the $\overline{\mathrm{PGF}_{y*}}$ is equatorward (i.e., preferential intrusion sites), its magnitude is $\approx 2-3\times10^{-6}$ m s^{-2}. This magnitude is comparable to the values obtained in the simplified experiments (Figure 10). The onshore velocities in the realistic experiment (simplified experiments) are typically 3–5 cm s^{-1} (1–4 cm s^{-1}).

The net transport across the TB shelf in the realistic experiment (EXP-smoo-3 experiment) is −0.13 Sv (−0.05 Sv). The difference is certainly in part due to the contribution of more energetic BC frontal eddies in the realistic experiment [see *Arruda et al.*, 2013 for details], since the BC sought in the simplified experiments is meant to represent a hypothetical state of the current with minimum eddy kinetic energy, i.e., least mesoscale activity.

5.2.2. Horizontal Patterns

After having examined the momentum budget along the shelf edge, a relevant question is: Is the equatorward PGF_{y*} also the primary forcing of the model intrusions inshore of the shelfbreak? To answer this, we examine the spatial distribution of the PGF_{y*} and the along-isobath Coriolis acceleration in the simplified experiments.

The onshore depth-averaged flow extends over large areas of the shelf in both EXP-smoo-1 (wind-only) and EXP-smoo-2 (BC–only) cases (Figure 12). These areas are consistent with the preferential intrusion sites discussed previously. The equatorward PGF_{y*} is partly balanced by the Coriolis acceleration, producing an onshore geostrophic flow. We also point out that the areas of onshore flow are roughly the same in both scenarios, once again suggesting that the effects of both forcings favor the SACW intrusions (Figures 12b and 12d), underneath the surface Ekman layer.

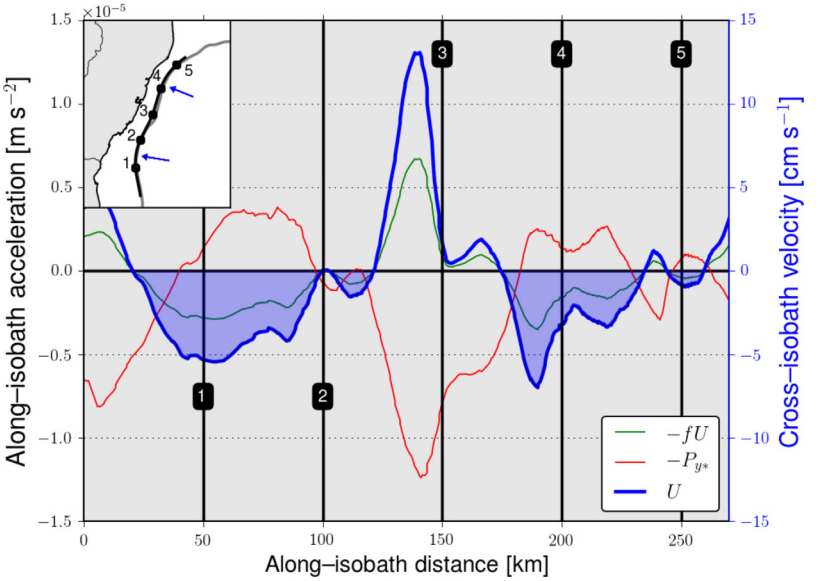

Figure 11. Time-averaged (2004–2009) and depth-averaged distributions of along-isobath pressure gradient force per unit mass ($-P_{y*}$), Coriolis acceleration ($-fU$), and cross-isobath velocity (U) along the 70 m isobath for the realistic experiment (HYCOM simulation). The blue-shading marks areas of onshore flow ($U < 0$), which are indicated by the blue arrows on the map insert. The vertical lines labeled 1–5 correspond to the dots on the 70 m contour of the map insert, which also shows the Brazilian coastal land mass (shaded).

Other studies have shown that preferential locations for offshore water intrusions and coastal upwelling may be associated with the combined effects of a western boundary current, upwelling-favorable winds and shelf geometry. Specifically, *Palma and Matano* [2009] show that a large area of geostrophically balanced equatorward PGF_{y*} forms in their numerical experiments in the South Brazil Bight area (22°S–28.5°S), producing onshore flow. At the south end of this region, *Campos et al*. [2013] show that the combination of intermittent upwelling-favorable winds and the BC-related PGF_{y*} is a plausible explanation for the observed prevalence of coastal upwelling off a particular location around Cape Santa Marta (28.5°S). In addition, the cape geometry has an important local effect in producing vertical transport through flow-topography interaction mechanisms [*Mazzini and Barth*, 2013]. The ESB area also features dramatic along-shelf changes in shelf geometry and coastline orientation, which have been shown to be important at smaller scales by *Mazzini and Barth* [2013]. The present study suggests conclusions consistent with this perspective, as both the wind and the BC forcings add up to produce onshore motion at the preferential locations indicated by the blue arrows in Figure 12.

5.3. Possible Causes of the Along-Isobath Pressure Gradients

The results presented in the previous section show that the key driver of SACW intrusions in the TB is ultimately the equatorward PGF_{y*} produced by the interactions of the wind-driven flow with the along-shelf changes in shelf topography and coastline geometry. One of the effects related to along-shelf topographic variability is that onshore transport during upwelling is expected to be enhanced in regions where the shelf narrows in the direction of long Coastal Trapped Wave (CTW) propagation [*Pringle*, 2002]. Since the downwave direction here is equatorward, the narrowing of the shelf northward of ≈22°S is expected to enhance onshore transport within the TB. Conversely, the sharp downwave widening of the shelf northward of ≈19.5°S is expected to inhibit onshore transport north of the TB (Figure 1a). Additional PGF_{y*}-related effects are the steering of the cross-isobath flow associated with wind-driven upwelling by the along-shelf varying bottom topography and steady lee wave-like circulation locked to abrupt topographic features. At larger scales, Arrested Topographic Wave physics (discussed in detail in section 6.4) may be important in spreading pressure gradients produced by other mechanisms.

Although it is beyond the scope of this study, we find that some of the mechanisms described above could also be rationalized in terms of potential vorticity conservation arguments. For example, the interplay between bottom friction torque and nonlinear vorticity advection discussed by *Liu and Gan* [2014] could be important near promontory-like features as in the north end of the TB (Figure 1a). On the other hand, within

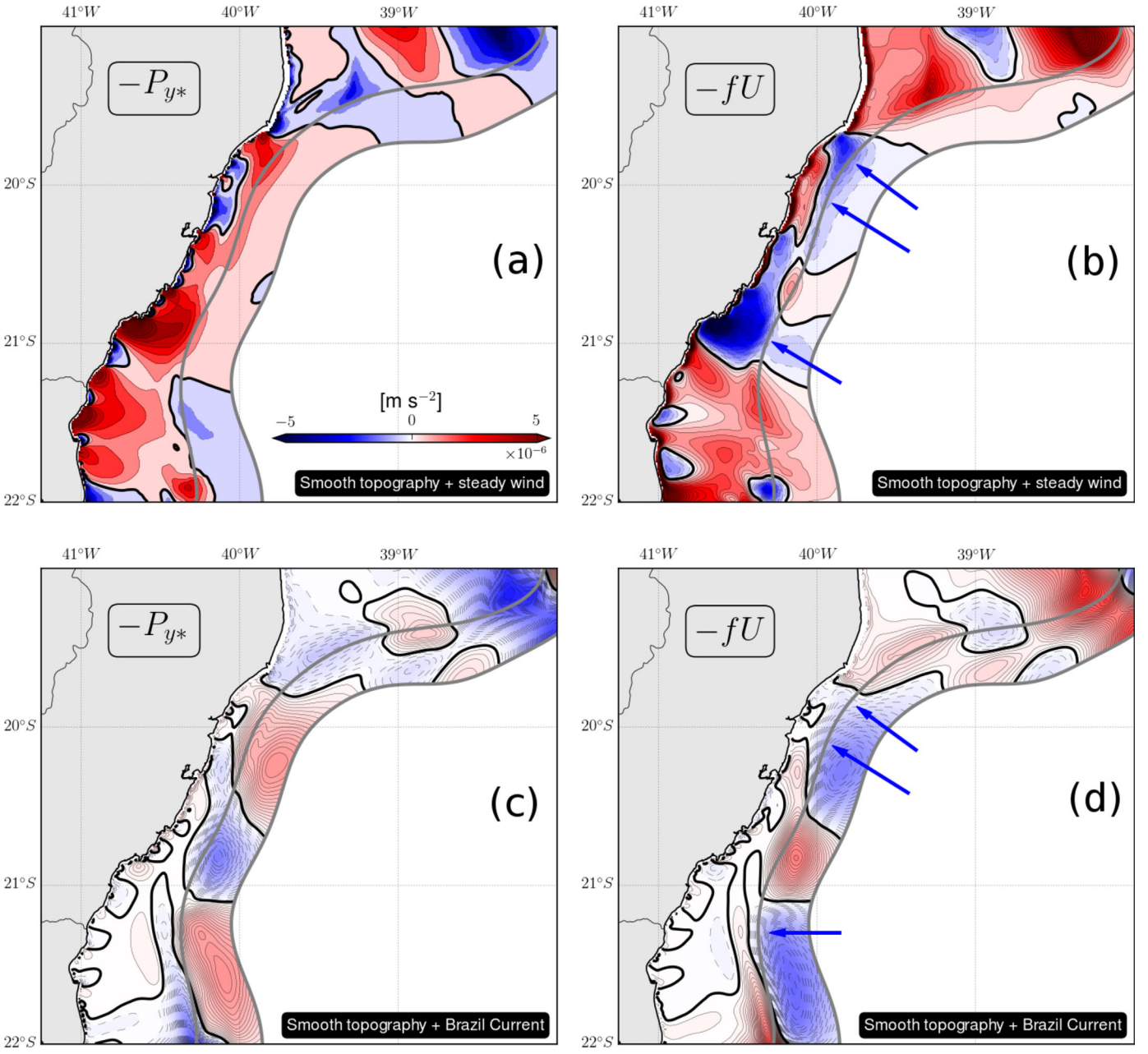

Figure 12. Horizontal distribution of run-averaged (30 days) and depth-averaged along-isobath pressure gradient force per unit mass ($-P_{y*}$, a, c) and Coriolis acceleration (–*fU*, b, d) for the smooth topography scenarios. (a, b) EXP-smoo-1 (wind–only). (c, d) EXP-smoo-2 (BC–only). The thick gray lines represent the 70 and 1000 m isobaths. The color scale is the same for all plots and the heavy black line is the zero contour. The blue arrows on the right column indicate preferential pathways of onshore flow.

the TB itself (where the shelf is essentially straight) nonlinear effects are expected to be weaker, and therefore the linear potential vorticity analysis of *Pringle* [2002] or the dynamics dominated mostly by bottom friction torque described in *Gan et al*. [2013] are expected to be more applicable to this region.

6. Deep-Ocean Forcing Mechanisms

In this section, we attempt to isolate some of the deep-ocean physical processes involved in the SACW intrusions. We begin by quantifying the change in the upwelling source water caused by the thermal wind signal of the BC. Next, we investigate the shelf encroaching of the BC by inertial overshooting and the

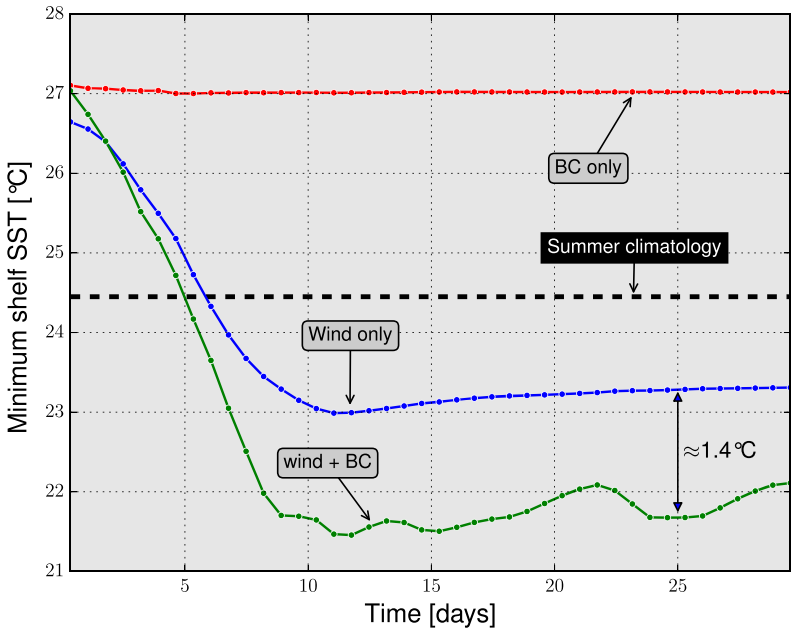

Figure 13. Comparison of the model minimum shelf Sea Surface Temperature (SST) histories (within the TB area) for EXP-smoo-1 (wind–only), EXP-smoo-2 (BC–only), and EXP-smoo-3 (wind+BC) experiments, demonstrating the effect of pycnocline uplifting by thermal wind shear of the BC jet. The black-dashed line indicates the observed climatological minimum SST.

along-shelf pressure gradient associated with the planetary β-effect. Finally, we use an Arrested Topographic Wave (ATW) model to rationalize the onshore spreading of the pressure gradients imparted by the BC along the shelf edge.

6.1. Pycnocline Uplifting Linked to the Brazil Current Mean Jet

Perhaps the simplest mechanism through which a boundary current can influence coastal and shelfbreak upwelling is by changing the properties of the water available at the shelf edge. This is a consequence of the fact that the current is in thermal wind balance, and therefore the pycnocline has to be either deeper or shallower (the present case) relative to its depth in the Sverdrup interior.

We quantified the change in the upwelling source water induced by the BC uplifting by comparing the minimum SST histories on the TB shelf in the simplified model experiments. Figure 13 shows that both wind-driven scenarios undergo a spin-up phase and attain a quasi-steady minimum shelf SST. In EXP-smoo-3 (wind+BC), however, the minimum SST is ≈1.4°C lower than in EXP-smoo-1 (wind-only). But is the upwelling source water colder in the wind+BC case because the isotherms are uplifted or just because the BC induces additional onshore transport by e.g., an enhanced equatorward PGF_{y^*} along the shelf edge? As discussed in section 5.2.1, the depth-averaged momentum balance along the shelf edge in the wind+BC case is very similar to that in the wind-only case. Specifically, in both cases the maximum equatorward PGF_{y^*} is $\approx 2\times10^{-6}$ m s^{-2} and the maximum onshore velocities are ≈3 cm s^{-1} (not shown). We therefore argue that the change in SST is mostly a consequence of the availability of colder water at the shelf edge due to the presence of the BC there.

6.2. Shelf Encroaching of the Brazil Current by Inertial Overshooting

When flow in exact geostrophic balance encounters a change in bottom topography, its ability to continue to follow isobaths depends on its amount of inertia. As it flows along the ESB shelfbreak, the BC is expected to locally overshoot it in some areas, thereby advecting SACW and TW onto the outer part of the continental shelf.

This effect is expected to be more important where the curvature R^{-1} of the isobaths is large enough to cause the centrifugal acceleration V^2/R experienced by a water parcel moving with an along-isobath velocity V to become comparable to the Coriolis acceleration fV. The ratio

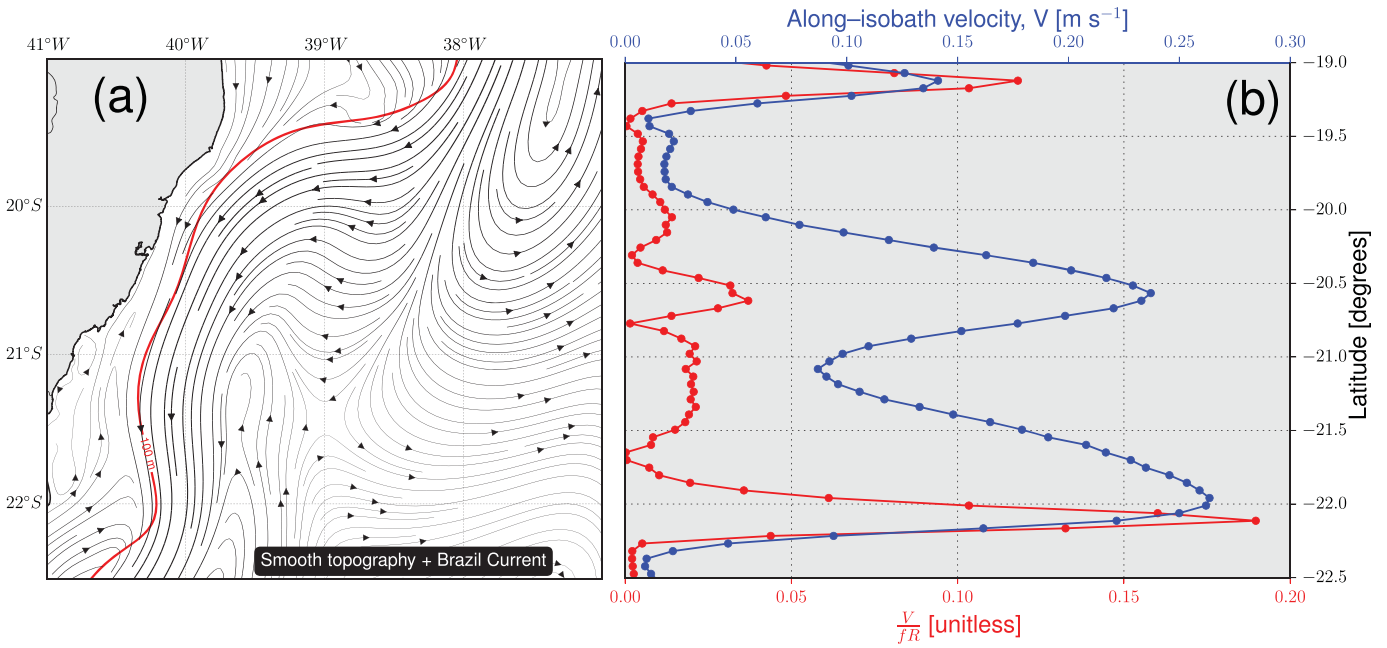

Figure 14. Distributions of model velocity (2004–2009 average and depth-averaged in the upper 100 m) and $Ro_{curv} = V/(fR)$ ratio (centrifugal acceleration normalized by the Coriolis acceleration). (a) Streamlines for process-oriented experiment EXP-smoo-2 (BC–only). The red line is the 100 m isobath, used to perform the Ro_{curv} calculations. (b) Associated along-isobath velocity (blue) and curvature Rossby number Ro_{curv} (red) as functions of latitude. The two Ro_{curv} maxima (near 19°S and 22°S) are areas where curvature effects are large, causing the BC jet to be more likely to encroach the shelf.

$$Ro_{curv} = \frac{V}{fR} \tag{6}$$

can therefore be defined to measure the contribution of curvature effects. Figure 14 shows Ro_{curv} along the 100 m isobath in EXP-smoo-2 as a function of latitude. The mean (maximum) value of Ro_{curv} is 0.02 (0.18), and the local maxima coincide with the areas of maximum isobath curvature. Away from the maxima, Ro_{curv} is everywhere smaller than 0.05. The smallness of Ro_{curv} reflects the relatively weak mean along-isobath flow in EXP-smoo-2, which is everywhere slower than 26 cm s^{-1}. If a synoptic along-isobath velocity of 0.6 m s^{-1} is considered instead (as observed during e.g., the OCT12 survey, not shown), the mean (maximum) Ro_{curv} increases to 0.10 (0.50). Curvature effects are hence more relevant in the south and north ends of the TB (larger curvature), especially when the incoming BC jet is more energetic.

Areas of high relative vorticity ζ clearly exist along the TB shelf edge, and a convenient measure of the relative importance of the total (curvature + shear) nonlinear effects is given by the quantity $Ro = |\zeta/f|$ (Figure 15). The time-mean realistic model field indicates typical (maximum) values of Ro of ≈0.3 (≈0.5), spreading over the TB slope and shelf edge. Therefore it seems that it is horizontal shear effects (rather than the more localized and episodic curvature effects) that account for the bulk of the nonlinearities at the shelf edge in a time-mean sense. It must be stressed, however, that this BC-induced effect is confined to the shelf edge area, and is not directly related to the circulation on the interior of the shelf.

The Kuroshio is perhaps one of the best documented examples of the inertial overshooting process [e.g., *Hsueh et al.*, 1996; *Vélez-Belchí et al.*, 2013], with Ro ≈ 0.5 [e.g., *Brink*, 1998]. The size of Ro estimated in the present analyses therefore predicts shelf encroaching to be locally important along the TB shelf edge. Moreover, the local SACW intrusions associated with this process are expected to facilitate further onshore geostrophic transport by the equatorward PGF_{y*}. For example, off southeast Australia, encroaching of the East Australian Current (EAC) has been shown to occasionally precondition the shelf stratification with colder offshore water, which may in turn reach the coast under the influence of persistent upwelling-favorable winds. This interaction has been shown to cause more intense coastal upwelling events than without encroaching or other upwelling-favorable EAC-related processes [e.g., *Gibbs et al.*, 1998; *Roughan and Middleton*, 2002; *Schaeffer et al.*, 2013]. Events where the BC is more energetic are thus probably associated with stronger shelf encroaching, and therefore more significant preconditioning of the shelf to wind-driven upwelling.

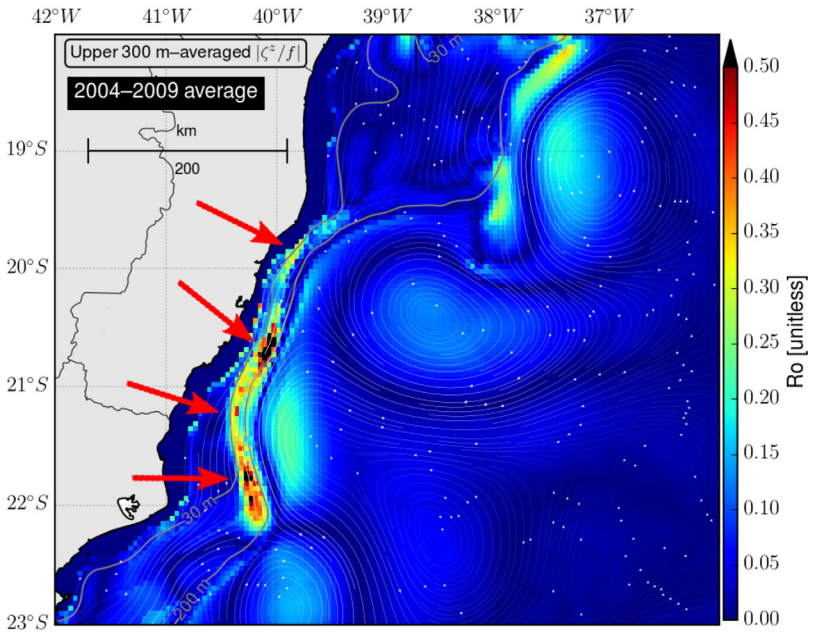

Figure 15. Distribution of 2004–2009 average of depth-averaged (within the upper 300 m) model relative vorticity normalized by the local inertial frequency, Ro=$|\zeta^z/f|$ (color shading) derived from the realistic HYCOM simulation, demonstrating the proneness of shelf edge areas to the effect of shelf encroaching of the BC. The white streamlines are the associated time and depth-averaged flow. The gray lines are the 30 and 200 m isobaths. The arrows indicate areas of large relative vorticity, located mostly along the shelf edge, following the inshore lobe of the BC jet.

6.3. Meridional Pressure Gradient Induced by the Planetary β-Effect

Although safely neglected in models of coastal circulation where the *f*-plane approximation is valid, the planetary β-effect is perhaps an overlooked mechanism in the context of shelfbreak upwelling. In the following, we examine the meridional (i.e., along-shelf) pressure gradient force PGF_y^β induced by the planetary β-effect. We employ a single-layer reduced gravity model (Figure 16) as in *Charney* [1955]. The dynamically active (upper) layer is assumed to be in geostrophic balance, i.e.,

$$-fv=-g'h_x, \tag{7}$$

where f is the Coriolis parameter, v is the along-shelf velocity, h is the upper layer thickness, and $g'\equiv g(\rho_2-\rho_1)/\rho_2$ is a reduced gravity based on the total acceleration due to gravity g and the densities of the upper (ρ_1) and lower (ρ_2) layers. The subscript x indicates partial differentiation in the cross-shelf direction. Multiplying equation (7) by h and integrating from the shelf edge ($x=x_c$) to the offshore limit of the western boundary layer ($x=x_o$) gives

$$\int_{x_c}^{x_o} hv\,dx=\frac{g'}{f}\int_{x_c}^{x_o} h_x h\,dx. \tag{8}$$

The left-hand side of equation (8) is the total along-shelf volume transport Q in the upper layer. Manipulating the right-hand side using the product rule yields

$$Q=\frac{g'}{f}\int_{x_c}^{x_o}(h^2/2)_x\,dx, \tag{9}$$

or, in terms of the thermocline depths at the outer limit of the BC (h_o) and at the shelf edge (h_c),

$$h_c^2=h_o^2-\frac{2fQ}{g'}. \tag{10}$$

Equation (10) establishes a relationship between the along-shelf transport of the BC and how much it uplifts the thermocline in the cross-shelf direction. We may now seek a crude estimate of the along-shelf pressure gradient force at the shelf edge (PGF_y^β) caused in response to this effect. We assume that the BC jet

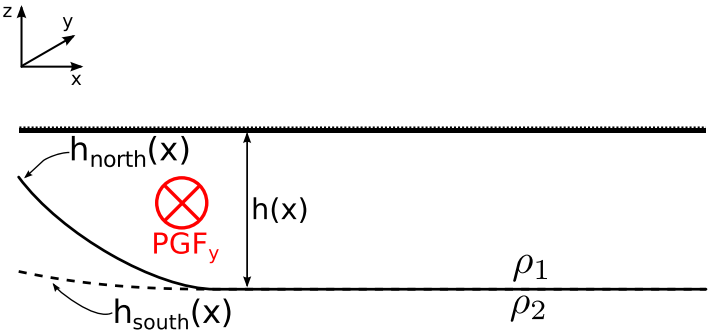

Figure 16. Schematic representation of a single-layer reduced gravity model for the BC. *x*, *y*, and *z* represent the cross-shelf, along-shelf, and vertical coordinate axes, respectively. $h(x)$ represents the thickness of the upper layer, and ρ_1 and ρ_2 represent the densities of the upper and lower layers, respectively. The shape of the layer interface at south (h_{south}) and north (h_{north}) locations and the associated equatorward pressure gradient force (PGF_y) are schematically depicted.

conserves mass (Q = constant) between two along-shelf locations y_{north} = 19° S and y_{south} = 22° S, and that the offshore thermocline depth h_o does not vary between those locations. Plugging in approximate values for Q, g', h_o, f_{north}, and f_{south} in equation (10) yields

$$(h_c)_{north} - (h_c)_{south} \approx -8 \text{ m}, \tag{11}$$

that is, the thermocline is predicted to be ≈8 m shallower in the north end of the TB shelf, which is consistent with the existence of a northward PGF_y^β and an onshore geostrophic flow across the shelf edge. We may use equation (11) to estimate the magnitude of this force:

$$PGF_y^\beta = -g'\left[\frac{(h_c)_{north} - (h_c)_{south}}{y_{north} - y_{south}}\right] = 5.6\times10^{-7} \text{ m s}^{-2}. \tag{12}$$

This mechanism is therefore predicted to drive an onshore depth-averaged geostrophic velocity PGF_y^β/f of ≈ -1 cm s^{-1}, which is smaller than the typical time-mean, depth-averaged onshore cross-isobath velocities found in the realistic numerical experiment (≈−5 cm s^{-1}, Figure 11). However, it should be pointed out that this is a permanent background forcing acting along the shelf edge.

6.4. Onshore Penetration of the Brazil Current Pressure Gradients

In section 5, the bulk of the onshore transport in the BC–only case was ascribed to a shelf-wide, geostrophically balanced, periodic pressure gradient force in the along-isobath direction. In this section, we investigate the cross-shelf penetration scales of the BC pressure gradients using a simple Arrested Topographic Wave (ATW) model.

6.4.1. The Analytical Model

We consider the idealized domain of a continental shelf in the southern hemisphere that is infinite in the meridional direction, with a solid coastal boundary at $x = 0$. A steady western boundary current flows poleward along the shelf edge, which is placed at $x = L$. The current has a periodic structure with wavelength $2\pi/l$ in the along-shelf direction. No wind forcing is prescribed.

Under the long-wave [e.g., *Gill and Schumann*, 1974] and *f*–plane approximations, the depth-averaged equations of motion in the steady, linear, and barotropic limits are [e.g., *Csanady*, 1978]:

$$-fv = -\frac{1}{\rho}p_x \tag{13}$$

$$fu = -\frac{1}{\rho}p_y - \frac{rv}{h} \tag{14}$$

$$(uh)_x + (vh)_y = 0, \tag{15}$$

where p is the depth-averaged pressure, u and v are the cross and along-shelf depth-averaged velocities, f is the Coriolis parameter, ρ = 1025 kg m^{-3} is density, r is a linear bottom resistance coefficient, and h is depth. A linear cross-shelf depth profile of the form $h = h_0 + sx$ is chosen, with h_0 = 0 m and $s > 0$. Subscripts with respect to the independent variables (x,y) indicate partial differentiation.

Equations (13), (14), and (15) may be combined into a single parabolic partial differential equation for pressure, i.e.,

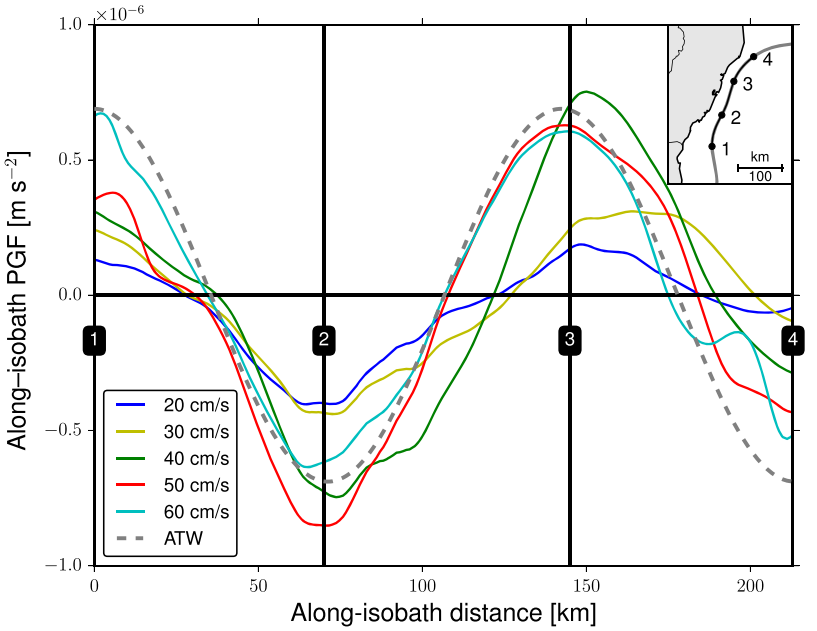

Figure 17. Numerical run-averaged (30 days) depth-averaged along-isobath Pressure Gradient Force (PGF) at the shelf edge (70 m isobath) as a function of along-isobath distance. Each line represents a numerical solution for a different BC core velocity. The gray-dashed line is a least squares sinusoidal fit representing the idealized forcing prescribed at the shelf edge of the ATW model. The vertical lines labelled 1–4 indicate along-isobath locations, which correspond to the numbered dots on the map insert.

$$p_{xx}+\frac{fs}{r}p_y=0. \tag{16}$$

As wind forcing is not included here, the boundary condition of no cross-shelf flow at the coast ($uh=0$ at $x=0$) that follows from equations (13) and (14) is

$$p_x=0. \tag{17}$$

The boundary condition at the shelf edge ($x=L$) is chosen to approximate the sinusoidal shape of the pressure field obtained in the numerical solutions (Figure 17):

$$p=a\sin(ly), \tag{18}$$

where a and l are the amplitude and along-shelf wavenumber of the pressure field, respectively.

Since we are only concerned with the onshore penetration of a prescribed sinusoidal field along the shelf edge, we neglect the boundary condition in the $\hat{y}$ direction. Defining $k\equiv -r/fs$, the problem becomes

$$p_y=kp_{xx} \tag{19}$$

$$p_x(0,y)=0 \tag{20}$$

$$p(L,y)=a\sin(ly) \tag{21}$$

in the domain $0<x<L$, $-\infty<y<+\infty$. The solution is (see Appendix A for details):

$$p(x,y)=\frac{ia}{2}\left\{\left[\frac{\cosh(\bar{z}qx)}{\cosh(\bar{z}qL)}\right]e^{-ily}-\left[\frac{\cosh(zqx)}{\cosh(zqL)}\right]e^{+ily}\right\}, \tag{22}$$

with $z\equiv(1+i)$, $\bar{z}\equiv(1-i)$ and $q\equiv\sqrt{l/(2k)}=\sqrt{-lfs/(2r)}$. We note that the e–folding scale of p in the cross-shelf direction (the real quantity $L_p\equiv q^{-1}$) does not depend on the amplitude a of the forcing. The distance L_p scales the onshore extent of deep-ocean influence in the case of periodic forcing at the shelf edge. This result is analogous to that of the periodic along-shelf wind stress ATW problem, where l represents the along-shelf wavenumber of the along-shelf component of the wind stress [*Csanady*, 1978; *Winant*, 1979].

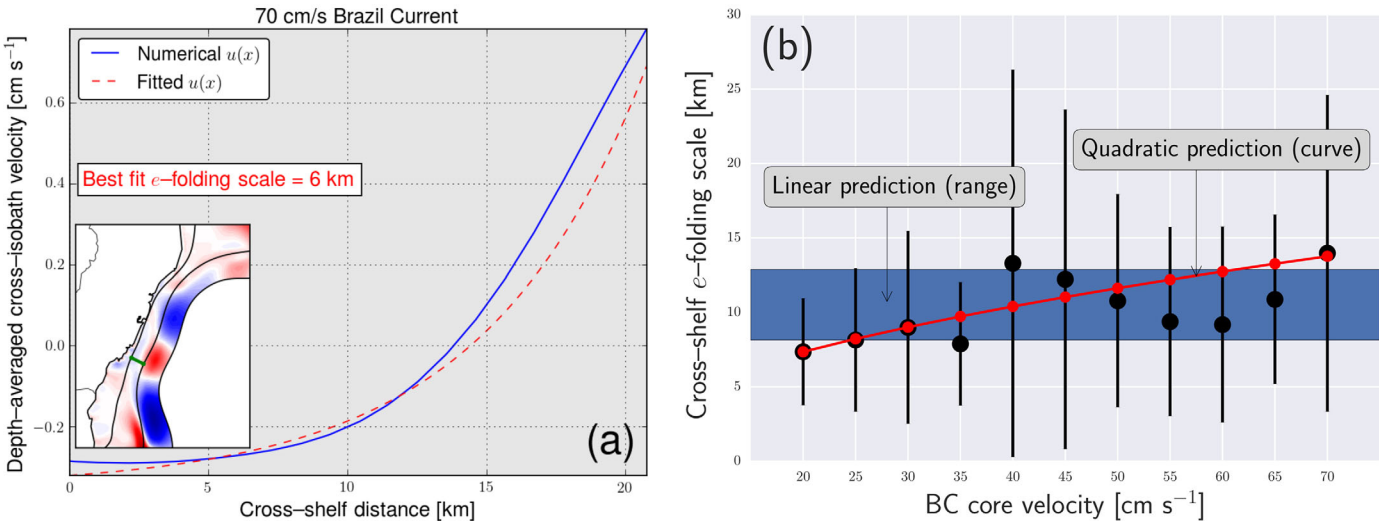

Figure 18. (a) Example of cross-shelf profile of depth-averaged, cross-isobath velocity *u* from a run-averaged (30 days) numerical solution (blue line) and associated exponential fit (dashed red line). The numerical *e*-folding scale estimated with a nonlinear least squares technique is shown. The map insert shows the location of the cross-shelf profile (green line) and the spatial distribution of *u* (color shading). Blue means onshore flow, red means offshore flow. (b) Shelf-averaged cross-shelf *e*-folding scales for cross-shelf velocity (black dots) estimated from the numerical solutions as a function of forcing amplitude (Brazil Current core velocity). The error bars indicate one standard deviation above and below each mean. The blue-shading marks the predicted range of onshore penetration scales $L_p=\sqrt{2k/l}=\sqrt{-2r/(lfs)}$, considering a canonical range for the linear bottom friction parameter *r* (from 2×10^{-4} to 5×10^{-4} m s^{-1}). The red curve marks the change in the quadratic onshore penetration scale $L_p^{\text{quadratic}}=\sqrt{-2C_D/(lfs)}\times\sqrt{U_{bot}}$, where $C_D=3.0\times10^{-3}$ is the quadratic bottom friction parameter used in the process-oriented numerical solutions and U_{bot} is the magnitude of the near-bottom velocity (assumed to be proportional to the model BC core velocity for simplicity). The red curve represents increments relative to the first numerical *e*-folding scale ($U_{\text{bot}}=20$ cm s^{-1}) rather than absolute values.

The choice of the parameters *a*, *l*, *f*, *s*, *r*, and *L* (-16 N m^{-2}, 4.42×10^{-5} m^{-1}, -5.10×10^{-5} s^{-1}, 2.68×10^{-3}, 3×10^{-4} m s^{-1}, and 25 km, respectively) was guided by the numerical solutions from experiment EXP-smoo-2 (see Figure 12 for an example of the shelf-wide spreading of the periodic along-isobath pressure gradient force) and the approximate geometry of the TB shelf. The meridional shelf length is $L^y\equiv214$ km (representative of the TB shelf), and the choice of pressure amplitude *a* corresponds to a reference amplitude of the numerical pressure gradient force (6.9×10^{-7} m s^{-2}). The along-shelf wave number $l=3\pi/L^y$ m^{-1} is set so as to simulate the numerical shelf edge pressure field (Figure 17). The linear drag coefficient *r* is picked from a range that has been found to agree well with observations [e.g., *Pringle*, 2002]. The predicted cross-shore scale of deep-ocean influence associated with these parameters is $L_p=\sqrt{-2r/(lfs)}=10$ km. For reference, the internal Rossby radius of deformation at the 70 m isobath is $L_d=NH/f=18$ km, using a mean *N* value for the TB shelf (Table 2).

6.4.2. Comparison With Primitive-Equation Numerical Solutions

We compare the analytical and numerical solutions in terms of the cross-shelf penetration scales. Figure 18a shows an example of cross-shelf profile of depth-averaged cross-isobath velocity (*u*), and the associated exponential fit. The length scale $L_p=\sqrt{2k/l}=\sqrt{-2r/(lfs)}$ predicted by the ATW solution for values of the linear bottom friction parameter *r* in the canonical range 2×10^{-4} – 5×10^{-4} m s^{-1} [e.g., *Pringle*, 2002] is consistent with the numerical results in terms of order of magnitude.

For a bulk comparison, we averaged all of the fit *e*-folding scales for ten cross-shelf lines within the TB to obtain a mean value and a standard deviation for each BC flow amplitude. Figure 18b shows that L_p has a general increasing dependence on the forcing amplitude, meaning that a stronger incoming BC flow tends to penetrate farther onshore. Evidently, the nonconstancy of the numerical penetration scales is partly attributable to the complexity of the primitive-equation model.

Another important source of disagreement is that the numerical solutions use a quadratic bottom stress parameterization, meaning that the equivalent of the linear bottom friction parameter *r* is the quantity C_DU_{bot}, where C_D is a unitless quadratic bottom friction parameter (set to 3.0×10^{-3} in the numerical solutions) and U_{bot} is the near-bottom velocity magnitude. Physically, this means that the predicted onshore penetration scale becomes a function of the forcing amplitude (i.e., the BC core velocity). This new penetration scale is thus

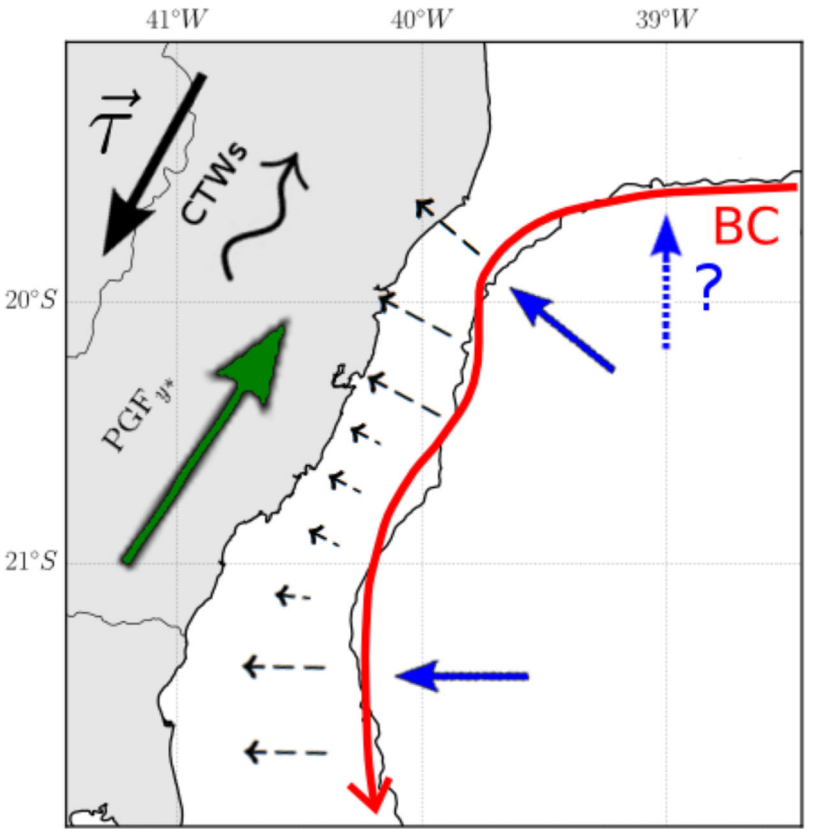

Figure 19. Schematic representation of the proposed South Atlantic Central Water (SACW) intrusion pathways and physical mechanisms in the Espírito Santo Basin shelf. The solid black arrow indicates the direction of prevailing wind and shelf mean flow. The wiggly arrow indicates the direction of propagation of long Coastal Trapped Waves (CTWs). The thick red line indicates the Brazil Current (BC) flow along the shelf edge and areas of local inertial overshooting. The blue arrows indicate preferential pathways for SACW intrusions. The dashed blue arrow indicates the possible pathway along the southern flank of the AB. The long (short) dashed black arrows over the shelf indicate areas of stronger (weaker) onshore flow. The green arrow indicates the direction of the total time-mean, along-isobath pressure gradient force (PGF_{y*}) on the shelf.

$$L_p^{\text{quadratic}} = \sqrt{\frac{-2C_D}{lfs}} \times \sqrt{U_{\text{bot}}}, \tag{23}$$

meaning that the onshore extent of deep-ocean influence over the shelf increases with the square root of U_{bot}. Assuming for simplicity that a change δU in the BC core velocity produces a change δU in U_{bot}, we use equation (23) to estimate the predicted change in $L_p^{\text{quadratic}}$. This change is relative to the first numerical solution (BC core velocity of 20 cm s^{-1}). We compare the result with the *e*-folding scales estimated from the numerical solutions and with the original ATW penetration scale L_p (Figure 18b).

The agreement between the numerical solutions and the theoretical predictions for the onshore penetration scales suggests that the ATW model is a plausible rationalization of the steady response of the coastal circulation to the sinusoidal BC forcing. The use of quadratic bottom stress accounts for some of the increase in the onshore penetration scale, improving the agreement between the analytical predictions and the numerical primitive-equation solutions. The weak (≈0.2–1.0 cm s^{-1}), shelf-wide cross-isobath ATW circulation could account for part of the onshore transport of cold, nutrient-rich SACW all the way across the shelf, provided that other physical processes have already transported it across the shelfbreak (e.g., inertial overshooting of the BC). This process could therefore be an additional supporting mechanism to the more energetic wind-driven cross-shelf circulation of SACW in the TB.

7. Summary and Conclusions

The goal of the present study is to investigate the intrusion pathways and the associated physical mechanisms involved in the intrusions of South Atlantic Central Water (SACW) on the Espírito Santo Basin (ESB)

shelf, with emphasis on the Tubarão Bight (TB) area. We employ a combination of process-oriented numerical experiments, an analysis of available observations, and simple analytical and conceptual models to examine the effects of bottom topography, wind forcing and the Brazil current (BC). A schematic overview of our findings is presented in Figure 19.

The regional picture that emerges from this study is that of a scale-dependent cross-shelf coastal circulation, which is wind-driven at leading order, but modulated by deep-ocean processes at next order. SACW appears to enter the model shelf through preferential pathways which coincide with along-shelf locations where a geostrophically balanced equatorward (i.e., intrusion-favorable) along-isobath pressure gradient force (PGF_{y*}) exists, as consistently suggested by the simplified and realistic numerical experiments. The geostrophic balance in the along-isobath direction is modified mostly by momentum advection at mid-depth and mostly by friction within the bottom Ekman layer. Both wind and BC-forced scenarios are found to produce an equatorward PGF_{y*}. However, the BC-induced PGF_{y*} is about half as intense as its wind-induced counterpart (which is $\approx 2\times10^{-6}$ m s^{-2}), and has a periodic along-shelf pattern, alternating areas of onshore and offshore geostrophic flow. The net effect is an equatorward PGF_{y*} throughout most of the TB, with local maxima at the preferential intrusion sites.

Typical magnitudes of the model time-mean, depth-averaged onshore velocities are 1–5 cm s^{-1}. The dominance of the model onshore geostrophic flow extends beyond the shelf edge area, apparently contributing to the SACW transport also on the shelf proper. Estimates of the slope Burger number S from the five available quasi-synoptic data sets yield values between 0.32 and 0.92. The vertical structure of the model onshore velocity at the shelf edge is consistent with theoretical predictions for $S \sim O(1)$, suggesting the interpretation that the cross-isobath velocity structure in the TB is modulated by the intensity of the SACW intrusions.

Wind forcing alone is both required and sufficient to reproduce the main features of coastal upwelling in the TB. Among the next-order effects, the uplifting of the thermocline by the BC results in the outcropping of water about 1.4°C colder under steady, upwelling-favorable wind forcing (compared to a flat stratification, BC-free scenario). The BC also affects the SACW intrusions by inertially overshooting the shelf edge, consistent with what is expected for the estimated Rossby numbers of about 0.3–0.5 along the shelf edge. In addition, the planetary β-effect is also predicted to account for a background equatorward PGF_{y*}, with magnitude comparable to that of the sinusoidal PGF_{y*} in the BC–only process-oriented experiments ($\approx 6\times10^{-7}$ m s^{-2}).

The effects of the BC in remotely setting up a shelf-wide PGF_{y*} are examined in the framework of a modified Arrested Topographic Wave (ATW) model. The onshore penetration scales of the time-mean sinusoidal PGF_{y*} found along the shelf edge in the experiments forced only by the BC are roughly predicted by the ATW cross-shelf e-folding scale $L_p = \sqrt{-2r/(lfs)} = 10$ km, where r is a linear bottom resistance parameter, l is the along-shelf wavenumber of the forcing at the shelf edge, f is the Coriolis parameter, and s is the bottom slope. Moreover, a modified form of this scale that uses a quadratic bottom stress parameterization (as prescribed in the numerical experiments) seems to account for some of the increase in the numerical penetration scale with the BC amplitude. This quadratic onshore penetration scale is $L_p^{\text{quadratic}} = \sqrt{-2C_D/(lfs)}\times\sqrt{U_{\text{bot}}}$, where C_D is a quadratic bottom friction parameter and U_{bot} is the near-bottom velocity magnitude. The kind of steady response to periodic deep-ocean forcing examined here may provide insight into other continental shelves under the influence of boundary currents or other deep-ocean low-frequency pressure forcings.

In closing, it should be stressed that it was not our intention to accurately represent the coastal and deep-ocean circulation in the ESB, nor to develop a detailed understanding of all the physical processes involved in the problem. Therefore, many open questions remain. Future work should be aimed at the effects on SACW intrusions of coastal trapped waves, internal waves, and the energetic mesoscale eddy field associated with the BC, among other processes. From an observational viewpoint, additional and better-resolved quasi-synoptic and moored observations on the middle shelf and shelf edge areas would allow for experimental testing of the model predictions discussed in the present study.

Appendix A: Solution of the ATW Problem

The problem posed in equations (19–21) is solved by assuming a periodic (in the $\hat{y}$ direction) solution of the form

$$p^{\pm}(x,y)=\phi^{\pm}(x)e^{\pm ily}, \tag{A1}$$

Such that the full solution is $p(x,y)=p^{+}(x,y)+p^{-}(x,y)$. Plugging A1 into equations (19–21) and using the fact that $a\sin(ly)=\frac{ia}{2}(e^{-ily}-e^{+ily})$, the following pair of boundary value problems is obtained:

$$\frac{d^2\phi^{\pm}}{dx^2}\mp\frac{il}{k}\phi^{\pm}=0 \tag{A2}$$

$$\frac{d\phi^{\pm}}{dx}(0)=0 \tag{A3}$$

$$\phi^{\pm}(L)=\mp\frac{ia}{2} \tag{A4}$$

The problems for the unknowns ϕ^{+} and ϕ^{-} are solved individually. Next, adding together the solutions for p^{+} and p^{-} gives the full solution for $p(x, y)$, i.e.,

$$p(x,y)=\frac{ia}{2}\left[\left(\frac{e^{+ibx}+e^{-ibx}}{e^{+ibL}+e^{-ibL}}\right)e^{-ily}-\left(\frac{e^{+bx}+e^{-bx}}{e^{+bL}+e^{-bL}}\right)e^{+ily}\right], \tag{A5}$$

with $b\equiv\sqrt{il/k}=(1+i)\sqrt{l/(2k)}$. Manipulating the exponents in equation (A5) yields the solution in the final form (equation (22)).

Appendix B: List of Acronyms

Main acronyms used in the text:

AB	Abrolhos Bank
ACR	Abrolhos–Campos Region
ATW	Arrested Topographic Wave
BC	Brazil Current
CF	Cape Frio
CST	Cape São Tomé
CTD	Conductivity, Temperature and Depth
EAC	East Australian Current
ESB	Espírito Santo Basin
FORMS	Feature–Oriented Regional Modeling System
HPGE	Horizontal Pressure Gradient Error
HYCOM	Hybrid Coordinate Ocean Model
PGF	Pressure Gradient Force
ROMS	Regional Ocean Modeling System
sSEC	Southern branch of the South Equatorial Current
SST	Sea Surface Temperature
TB	Tubarão Bight
TW	Tropical Water
VTR	Vitória–Trindade Ridge
WOA13	World Ocean Atlas 2013

Acknowledgments

The first author acknowledges support from the São Paulo Research Foundation (*Fundação de Amparo à Pesquisa do Estado de São Paulo*, FAPESP), via grants 2013/11465–4 and 2014/03451–6. Kenneth Brink acknowledges support from NSF (grant OCE-1433953). Ilson da Silveira acknowledges support from FAPESP 08/58101–9, CNPq 3071122/2010–7, and CAPES 2201/2014. Wilton Arruda acknowledges support from CNPq (MCTI/CNPq/Universal 14/2014, grant 443162/2014–0), and from INCT–Mar–COI, MCTI/CNPq grant 565062/2010–7. Renato Martins acknowledges support from Petróleo Brasileiro S/A (AMBES Project, PT–133.01.10636). Suggestions regarding ROMS momentum balance diagnosis from Professor Jianping Gan (HKUST/China) and suggestions on model implementation from Deepak Cherian (WHOI) are gratefully acknowledged. Thanks are also due to Professors Steven Lentz (WHOI) and Belmiro Castro (IO/USP) for insightful comments and suggestions. The PRO–ABROLHOS cruise data were obtained from the LaDO–IO/USP historical database, and are available from the third author upon request (ilson.silveira@usp.br). The World Ocean Atlas 2013 climatological data (WOA13) was downloaded from https://www.nodc.noaa.gov/OC5/woa13/woa13data.html. The SRTM30–plus bottom topography data set was downloaded from http://topex.ucsd.edu/www_html/srtm30_plus.html. The Sea Surface Temperature climatology from the Pathfinder Project v5.0 was obtained at http://www.nodc.noaa.gov/SatelliteData/pathfinder4km/. The *Multiple–Satellite Blended Sea Surface Winds* product was downloaded from http://www.ncdc.noaa.gov/thredds/dodsC/oceanwinds. Data from the Abrolhos 1, Abrolhos 2, AMBES–09, and AMBES–10 surveys are property of Petróleo Brasileiro S/A, and may be purchased upon request to the fifth author (renatopm@petrobras.com.br). Due to this collaboration, this work is part of the AMBES Project. All model fields and software used in this work are available from the first author upon request (apaloczy@ucsd.edu).

References

Aguiar, A. L., M. Cirano, J. Pereira, and M. Marta-Almeida (2014), Upwelling processes along a western boundary current in the Abrolhos–Campos region of Brazil, *Cont. Shelf Res.*, *85*, 42–59.

Arruda, W. Z., E. J. D. Campos, V. Zharkov, R. G. Soutelino, and I. C. A. Da Silveira (2013), Events of equatorward translation of the Vitória Eddy, *Cont. Shelf Res.*, *70*, 61–73, doi:10.1016/j.csr.2013.05.004.

Beckmann, A., and D. B. Haidvogel (1993), Numerical simulation of flow around a tall isolated seamount. Part I: Problem formulation and model accuracy, *J. Phys. Oceanogr.*, *23*(8), 1736–1753.

Boebel, O., R. Davis, M. Ollitrault, R. Peterson, P. Richardson, C. Schmid, and W. Zenk (1999), The intermediate depth circulation of the western South Atlantic, *Geophys. Res. Lett.*, *26*(21), 3329–3332.

Brink, K. H. (1998), Deep–sea forcing and exchange processes, in *The Sea*, vol. 10, edited by K. H. Brink and A. R. Robinson, chap. 6, pp. 151–167, John Wiley, N. Y.

Brink, K. H. (2012), Buoyancy arrest and shelf–ocean exchange, *J. Phys. Oceanogr.*, *42*(4), 644–658.

Brink, K. H., and S. J. Lentz (2010), Buoyancy arrest and bottom Ekman transport. Part I: Steady flow, *J. Phys. Oceanogr.*, *40*(4), 621–635.
Calado, L., I. C. A. Silveira, A. Gangopadhyay, and B. M. Castro (2010), Eddy–induced upwelling off Cape São Tomé (22°S, Brazil), *Cont. Shelf Res.*, *30*(10–11), 1181–1188.
Campos, E. J. (2006), Equatorward translation of the Vitória Eddy in a numerical simulation, *Geophys. Res. Lett.*, *33*, L22607, doi:10.1029/2006GL026997.
Campos, P. C., O. Möller, A. R. Piola, and E. D. Palma (2013), Seasonal variability and coastal upwelling near Cape Santa Marta (Brazil), *J. Geophys. Res. Oceans*, *118*, 1420–1433, doi:10.1002/jgrc.20131.
Casey, K. S., T. B. Brandon, P. Cornillon, and R. Evans (2010), The past, present, and future of the AVHRR Pathfinder SST Program, in *Oceanography From Space*, edited by V. Barale, J. F. R. Gower, and L. Alberotanza, pp. 273–287, Springer, Dordrecht, Netherlands, doi:10.1007/978-90-481-8681-5_16.
Castelão, R. M., and J. A. Barth (2006), Upwelling around Cabo Frio, Brazil: The importance of wind stress curl, *Geophys. Res. Lett.*, *33*, L03602, doi:10.1029/2005GL025182.
Castro, B. M., and L. B. Miranda (1998), Physical Oceanography of the Western Atlantic Continental Shelf located between 4°N and 34°S, in *The Sea*, vol. 11, edited by A. R. Robinson and K. H. Brink, chap. 8, pp. 209–251, Wiley, N. J.
Castro, B. M., J. A. Lorenzetti, I. C. A. Silveira, and L. B. Miranda (2006), *O Ambiente Oceanográfico da Plataforma Continental e do Talude na Região Sudeste–Sul do Brasil [in Portuguese]*, 1st ed., chap. 1, pp. 11–120, EdUSP, São Paulo, Brazil.
Cerda, C., and B. M. Castro (2014), Hydrographic climatology of South Brazil Bight shelf waters between Sao Sebastiao (24°S) and Cabo Sao Tome (22°S), *Cont. Shelf Res.*, *89*, 5–14.
Charney, J. G. (1955), The Gulf Stream as an inertial boundary layer, *Proc. Natl. Acad. Sci. U. S. A.*, *41*(10), 731–740.
Clarke, A. J., and K. H. Brink (1985), The response of stratified, frictional flow of shelf and slope waters to fluctuating large–scale, low–frequency wind forcing, *J. Phys. Oceanogr.*, *15*(4), 439–453.
Csanady, G. T. (1978), The arrested topographic wave, *J. Phys. Oceanogr.*, *8*(1), 47–62.
Csanady, G. T. (1982), *Circulation in the Coastal Ocean*, 1st ed., D. Reidel, Reidel, Dordrecht, Netherlands.
Dottori, M., and B. M. Castro (2009), The response of the Sao Paulo Continental Shelf, Brazil, to synoptic winds, *Ocean Dyn.*, *59*(4), 603–614.
Evans, D. L., S. R. Signorini, and L. B. Miranda (1983), A note on the transport of the Brazil Current, *J. Phys. Oceanogr.*, *13*(9), 1732–1738.
Gaeta, S. A., J. A. Lorenzzetti, L. B. Miranda, S. M. Susini-Ribeiro, M. Pompeu, and C. E. Araujo (1999), The Vitória Eddy and its relation to the phytoplankton biomass and primary productivity during the austral fall of 1995, *Arch. Fish. Mar. Res.*, *47*(2/3), 253–270.
Gan, J., A. Cheung, X. Guo, and L. Li (2009), Intensified upwelling over a widened shelf in the northeastern South China Sea, *J. Geophys. Res.*, *114*, C09019, doi:10.1029/2007JC004660.
Gan, J., H. San Ho, and L. Liang (2013), Dynamics of intensified downwelling circulation over a widened shelf in the northeastern South China Sea, *J. Phys. Oceanogr.*, *43*(1), 80–94.
Gangopadhyay, A., and A. R. Robinson (2002), Feature–oriented regional modeling of oceanic fronts, *Dyn. Atmos. Oceans*, *36*(1), 201–232.
Garrett, C., P. MacCready, and P. Rhines (1993), Boundary mixing and arrested Ekman layers: Rotating stratified flow near a sloping boundary, *Annu. Rev. Fluid. Mech.*, *25*(1), 291–323.
Gibbs, M. T., J. H. Middleton, and P. Marchesiello (1998), Baroclinic response of Sydney shelf waters to local wind and deep ocean forcing, *J. Phys. Oceanogr.*, *28*(2), 178–190.
Gill, A. E., and E. H. Schumann (1974), The generation of long shelf waves by the wind, *J. Phys. Oceanogr.*, *4*(1), 83–90.
Haney, R. L. (1991), On the pressure gradient force over steep topography in sigma coordinate ocean models, *J. Phys. Oceanogr.*, *21*(4), 610–619.
Houry, S., E. Dombrowsky, P. De Mey, and J.-F. Minster (1987), Brunt-Väisälä frequency and Rossby radii in the South Atlantic, *J. Phys. Oceanogr.*, *17*(10), 1619–1626.
Hsueh, Y., H.-J. Lie, and H. Ichikawa (1996), On the branching of the Kuroshio west of Kyushu, *J. Geophys. Res.*, *101*(C2), 3851–3857.
Large, W. G., and S. Pond (1981), Open ocean momentum flux measurements in moderate to strong winds, *J. Phys. Oceanogr.*, *11*(3), 324–336.
Legeais, J.-F., M. Ollitrault, and M. Arhan (2013), Lagrangian observations in the intermediate western boundary current of the South Atlantic, *Deep Sea Res., Part II*, *85*, 109–126.
Lentz, S. J., and D. C. Chapman (2004), The importance of nonlinear cross–shelf momentum flux during wind–driven coastal upwelling, *J. Phys. Oceanogr.*, *34*(11), 2444–2457.
Liu, Z., and J. Gan (2014), Modeling study of variable upwelling circulation in the East China Sea: Response to a coastal promontory, *J. Phys. Oceanogr.*, *44*(4), 1078–1094.
Locarnini, R. A., et al. (2013), *World Ocean Atlas 2013, Vol. 1: Temperature*, edited by A. Mishonov, *NOAA Atlas NESDIS, 73*, 40 pp.
Lozano, C. J., A. R. Robinson, H. G. Arango, A. Gangopadhyay, Q. Sloan, P. J. Haley, L. Anderson, and W. Leslie (1996), An interdisciplinary ocean prediction system: Assimilation strategies and structured data models, *Elsevier Oceanogr. Ser.*, *61*, 413–452.
Mazzini, P. L. F., and J. A. Barth (2013), A comparison of mechanisms generating vertical transport in the Brazilian coastal upwelling regions, *J. Geophys. Res. Oceans*, *118*, 5977–5993, doi:10.1002/2013JC008924.
McCabe, R. M., B. M. Hickey, E. P. Dever, and P. MacCready (2015), Seasonal cross–shelf flow structure, upwelling relaxation, and the along-shelf pressure gradient in the northern California current system, *J. Phys. Oceanogr.*, *45*(1), 209–227.
McTaggart, K. E., G. C. Johnson, M. C. Johnson, F. M. Delahoyde, and J. H. Swift (2010), Notes on CTD/O_2 data acquisition and processing using Sea-Bird hardware and software (as available), The GO-SHIP Repeat Hydrography Manual: A Collection of Expert Reports and Guidelines, IOCCP Report 15.
Mémery, L., M. Arhan, X. A. Alvarez-Salgado, M.-J. Messia, H. Mercier, C. G. Castro, and A. F. Rios (2000), The water masses along the western boundary of the south and equatorial Atlantic, *Prog. Oceanogr.*, *47*(1), 69–98.
Miranda, L. B., and B. M. Castro (1982), Geostrophic flow conditions of the Brazil Current at 19°S, *Ciênc. Interam.*, *22*(1–2), 44–48.
Palma, E. D., and R. P. Matano (2009), Disentangling the upwelling mechanisms of the South Brazil Bight, *Cont. Shelf Res.*, *29*(11), 1525–1534.
Palma, E. D., R. P. Matano, and A. R. Piola (2008), A numerical study of the Southwestern Atlantic Shelf circulation: Stratified ocean response to local and offshore forcing, *J. Geophys. Res.*, *113*, C11010, doi:10.1029/2007JC004720.
Palóczy, A., I. C. A. Silveira, B. M. Castro, and L. Calado (2014), Coastal upwelling off Cape São Tomé (22°S, Brazil): The supporting role of deep ocean processes, *Cont. Shelf Res.*, *89*, 38–50.
Pereira, A. F., A. L. Belém, B. M. Castro, and R. Geremias (2005), Tide–topography interaction along the eastern Brazilian shelf, *Cont. Shelf Res.*, *25*(12), 1521–1539.
Pringle, J. M. (2002), Enhancement of wind–driven upwelling and downwelling by alongshore bathymetric variability, *J. Phys. Oceanogr.*, *32*(11), 3101–3112.

Pringle, J. M., and E. P. Dever (2009), Dynamics of wind–driven upwelling and relaxation between Monterey Bay and Point Arena: Local–, regional–, and gyre–scale controls, *J. Geophys. Res.*, *114*, C07003, doi:10.1029/2008JC005016.
Rodrigues, R. R., and J. A. Lorenzzetti (2001), A numerical study of the effects of bottom topography and coastline geometry on the Southeast Brazilian coastal upwelling, *Cont. Shelf Res.*, *21*(4), 371–349.
Rodrigues, R. R., L. M. Rothstein, and M. Wimbush (2007), Seasonal variability of the South Equatorial Current bifurcation in the Atlantic Ocean: A numerical study, *J. Phys. Oceanogr.*, *37*(1), 16–30.
Roughan, M., and J. H. Middleton (2002), A comparison of observed upwelling mechanisms off the east coast of Australia, *Cont. Shelf Res.*, *22*(17), 2551–2572.
Schaeffer, A., M. Roughan, and B. D. Morris (2013), Cross–shelf dynamics in a western boundary current regime: Implications for upwelling, *J. Phys. Oceanogr.*, *43*(5), 1042–1059.
Schmid, C., H. Schäfer, G. Podestà, and W. Zenk (1995), The Vitória eddy and its relation to the Brazil Current, *J. Phys. Oceanogr.*, *25*(11), 2532–2546.
Scott, J. T., and G. T. Csanady (1976), Nearshore currents off Long Island, *J. Geophys. Res.*, *81*(30), 5401–5409.
Shchepetkin, A. F., and J. C. McWilliams (2005), The regional oceanic modeling system (ROMS): A split–explicit, free–surface, topography–following–coordinate oceanic model, *Ocean Modell.*, *9*(4), 347–404.
Silveira, I. C. A., J. A. M. Lima, A. C. K. Schmidt, W. Ceccopieri, A. Sartori, C. P. F. Franscisco, and R. F. C. Fontes (2008), Is the meander growth in the Brazil Current system off Southeast Brazil due to baroclinic instability?, *Dyn. Atmos. Oceans*, *45*(3), 187–207.
Smith, W. H. F., and D. T. Sandwell (1997), Global sea floor topography from satellite altimetry and ship depth soundings, *Science*, *277*(5334), 1956–1962.
Soutelino, R. G., I. C. A. Silveira, A. Gangopadhyay, and J. A. Miranda (2011), Is the Brazil Current eddy–dominated to the north of 20°S?, *Geophys. Res. Lett.*, *38*, L03607, doi:10.1029/2010GL046276.
Soutelino, R. G., A. Gangopadhyay, and I. C. A. da Silveira (2013), The roles of vertical shear and topography on the eddy formation near the site of origin of the Brazil Current, *Cont. Shelf Res.*, *70*, 46–60, doi:10.1016/j.csr.2013.10.001.
Stech, J. L., and J. A. Lorenzzetti (1992), The response of the South Brazil Bight to the passage of wintertime cold fronts, *J. Geophys. Res.*, *97*(C6), 9507–9520.
Stramma, L., and M. England (1999), On the water masses and mean circulation of the South Atlantic Ocean, *J. Geophys. Res.*, *104*(C9), 20,863–20,883.
Stramma, L., Y. Ikeda, and R. G. Peterson (1990), Geostrophic transport in the Brazil Current region north of 20°S, *Deep Sea Res., Part A*, *37*(12), 1875–1886.
Trenberth, K. E., W. G. Large, and J. G. Olson (1990), The mean annual cycle in global ocean wind stress, *J. Phys. Oceanogr.*, *20*, 1742–1760.
Vélez-Belchí, P., L. R. Centurioni, D.-K. Lee, S. Jan, and P. P. Niiler (2013), Eddy induced Kuroshio intrusions onto the continental shelf of the East China Sea, *J. Mar. Res.*, *71*(1-2), 83–107.
Warner, J. C., J. H. List, W. C. Schwab, G. Voulgaris, B. Armstrong, and N. Marshall (2014), Inner–shelf circulation and sediment dynamics on a series of shoreface–connected ridges offshore of Fire Island, *Ocean Dyn.*, *64*(12), 1767–1781.
Wijesekera, H. W., J. S. Allen, and P. A. Newberger (2003), Modeling study of turbulent mixing over the continental shelf: Comparison of turbulent closure schemes, *J. Geophys. Res.*, *108*(C3), 3103, doi:10.1029/2001JC001234.
Winant, C. D. (1979), Comments on The Arrested Topographic Wave, *J. Phys. Oceanogr.*, *9*(5), 1042–1043.
Xu, J., R. J. Lowe, G. N. Ivey, N. L. Jones, and R. Brinkman (2015), Observations of the shelf circulation dynamics along Ningaloo Reef, Western Australia during the austral spring and summer, *Cont. Shelf Res.*, *95*, 54–73.
Zhang, H. M., J. J. Bates, and R. W. Reynolds (2006), Assessment of composite global sampling: Sea surface wind speed, *Geophys. Res. Lett.*, *33*(17), L17714, doi:10.1029/2006GL027086.
Zweng, M. M., et al. (2013), *World Ocean Atlas 2013, Volume 2: Salinity*, edited by S. Levitus and A. Mishonov, *NOAA Atlas NESDIS, 74*, 39 pp.